Phase Equilibrium Constraints on Pre-eruptive Conditions of Recent Felsic Explosive Volcanism at Pantelleria Island, Italy

Ida Di Carlo, Silvio G. Rotolo, Bruno Scaillet, Vincenzo Buccheri, Michel Pichavant

JOURNAL OF PETROLOGY | VOLUME 51 | NUMBER 11 | PAGES 2245–2276 | 2010 | doi:10.1093/petrology/egq055

Phase Equilibrium Constraints on Pre-eruptive Conditions of Recent Felsic Explosive Volcanism at Pantelleria Island, Italy

IDA DI CARLO[1,2], SILVIO G. ROTOLO[1], BRUNO SCAILLET[2]*, VINCENZO BUCCHERI[1] AND MICHEL PICHAVANT[2]

[1]UNIVERSITA DI PALERMO, DIPARTIMENTO DI CHIMICA E FISICA DELLA TERRA, VIA ARCHIRAFI 36, 90123 PALERMO, ITALY

[2]CNRS/INSU, UNIVERSITÉ D'ORLEANS, UNIVERSITÉ FRANÇOIS RABELAIS DE TOURS, INSTITUT DES SCIENCES DE LA TERRE D'ORLÉANS UMR 6113, 1A RUE DE LA FÉROLLERIE, 45071 ORLÉANS CEDEX 2, FRANCE

RECEIVED FEBRUARY 4, 2010; ACCEPTED AUGUST 27, 2010

We present experimental phase equilibria carried out on a pantelleritic bulk-rock composition with a peralkalinity index [PI = molar $(Na_2O + K_2O)/Al_2O_3$] = 1·4, which is representative of the most energetic pumice fall eruption of the resurgent post-caldera volcanism on Pantelleria island. For the explored conditions (P = 25–150 MPa; T = 680–800°C; H_2O_{melt} up to 6 wt %; $fO_2 \leq NNO$, where NNO is nickel–nickel oxide buffer) clinopyroxene is the liquidus phase followed by alkali feldspar and then quartz. The crystallization of amphibole is limited to temperatures below 700°C. Aenigmatite crystallizes near the liquidus for P ≥ 100 MPa. When clinopyroxene is the sole liquidus phase, the coexisting melt is characterized by a decrease in peralkalinity index to 1·2, if compared with the starting material, approaching comendite composition. In contrast, when alkali feldspar joins the liquidus phase assemblage, residual melts become extremely peralkaline (PI = 3·2), with FeO contents in excess of 14 wt %. Comparison of our experiments with natural phase abundances and compositions constrains the depth of the Fastuca pantellerite reservoir to be around 5 ± 1 km (or P = 120 ± 20 MPa) at T = 730 ± 10°C, with H_2O_{melt} around 4 wt %, and fO_2 1·5 log unit below NNO. Such conditions correspond to the dominant phase assemblage of feldspar, clinopyroxene and aenigmatite. Amphibole occurrence requires both higher melt water contents and lower temperatures (up to 6·5 wt % at 680°C), and may reflect provenance from a deeper and wetter portion of the tapped reservoir. In contrast, quartz is more probably related to crystallization during magma ascent, which explains the lower melt water content of its melt inclusions. Overall, the results confirm that pantellerites may be both water-rich and reduced magmas. These characteristics imply that any coexisting fluid phase in the reservoir will be dominated by water and hydrogen species, the latter amounting to a few mole per cent. Magma unrest at Pantelleria may thus be heralded by emissions of hydrous and reduced gases (i.e. CO_2-poor and H_2-rich), if the present-day reservoir is felsic in composition.

KEY WORDS: *peralkaline magmatism; phase equilibria; pantellerite; Pantelleria; hydrous reduced magma*

INTRODUCTION

Pantelleria island is the type-locality of pantellerite, an iron- and sodium-rich peralkaline rhyolite. Pantellerites, by far the most abundant rock-type at Pantelleria, occur as pyroclastic flows, pumice fall deposits, or as obsidianaceous lavas (Mahood & Hildreth, 1986). After the Plinian eruption of the Green Tuff (45 ka BP), and the related caldera collapse, resurgent felsic magmatism was mainly centered inside the caldera, producing either low-energy explosive eruptions or lava flows.

Recent experimental investigations (Scaillet & Macdonald, 2001, 2003) and melt inclusion studies (Kovalenko *et al.*, 1988; Webster *et al.*, 1993; Wilding *et al.*,

*Corresponding author. E-mail: bscaille@cnrs-orleans.fr

1993; Barclay *et al.*, 1996; Gioncada & Landi, 2010) have shown that peralkaline melts may be rather H_2O-rich, in contrast to previous inferences. These studies have also demonstrated the role of pressure, water, oxygen fugacity, and silica and sodium disilicate activity (aSiO$_2$, aNds) on the phase equilibria of felsic peralkaline magmas from the east Kenyan rift zone (e.g. Scaillet & Macdonald, 2001, 2003, 2006; Caricchi *et al.*, 2006).

In this study we present the hydrous phase equilibria of a pantellerite with a peralkalinity index PI [$=$ molar $(Na_2O + K_2O)/Al_2O_3] = 1{\cdot}4$, established within the pressure range 25–150 MPa, for temperatures between 680 and 800°C, with oxygen fugacities below the Ni–NiO solid buffer (NNO), and melt water contents (H_2O_{melt}) up to 6 wt %. We apply our experimentally derived P–T–H_2O_{melt} grid to natural pantellerites to assess the pre-eruptive conditions (T, P, H_2O_{melt}) of the most powerful event of the post-caldera period, the Fastuca eruption (Orsi *et al.*, 1989). Knowledge of the pre-eruptive conditions sheds light on the nature of the magmatic plumbing system associated with recent felsic volcanism at Pantelleria, with several obvious implications for the eruptive style of pantellerite magmas. The determination of magma storage conditions of pantelleritic magmas can also provide constraints on the more general problem of the origin of silica-oversaturated peralkaline magmas, which has been extensively debated (see Bohrson & Reid, 1997; Civetta *et al.*, 1998; Marshall *et al.*, 1998; Marshall *et al.* 2009; Scaillet & Macdonald, 2001; Nekvasil *et al.*, 2004; Macdonald *et al.*, 2008). Much of the controversy has arisen because of the lack of modern phase equilibrium constraints for peralkaline magmas, in contrast to their metaluminous or peraluminous counterparts (e.g. Scaillet *et al.*, 1995; Dall'Agnol *et al.*, 1999; Klimm *et al.*, 2003; Bogaerts *et al.*, 2006).

GEOLOGICAL AND PETROLOGICAL BACKGROUND

Pantelleria (Italy) is an entirely volcanic island (Fig. 1) located within the Sicily Channel continental rift system, in the northern part of the African plate (e.g. Rotolo *et al.*, 2006). Pantelleria is well known in the petrological literature because its eruptive products represent a typical bimodal suite: a mafic end-member, which consists of mildly alkali basalts, and a felsic end-member consisting of trachytes (metaluminous or slightly peralkaline) and pantellerites (PI $= 1{\cdot}2$–$2{\cdot}3$). Intermediate products between the mafic and felsic end-members do not occur as flow or fall units, having been found only as enclaves within the felsic rocks (Villari, 1974; Civetta *et al.*, 1984; Avanzinelli *et al.*, 2004; Ferla & Meli, 2006).

The early eruptive history of Pantelleria is mainly characterized by large explosive pantellerite or trachyte eruptions that produced at least four ignimbrite units, of which at least two resulted in caldera collapse. The latest among them was the Plinian eruption of the Green Tuff, which formed the Cinque Denti caldera, which occurred 45 ka BP (see Mahood & Hildreth, 1986, and references therein). After the Green Tuff eruption, a rather prolonged period of effusive activity formed the trachytic lava pile of Mt. Grande. Subsequently, the eruptive style shifted to one of low-energy strombolian-like eruptions of pantellerite magma, possibly associated with effusive events, resulting in a complex interfingering of pumice fall sequences, lava flows and lava domes (Rotolo *et al.*, 2007). This mildly explosive silicic activity was centered entirely within the caldera. On the other hand, the eruption of basaltic magmas (scoria cones, lava flows) was limited to the northern portion of the island. Among the recent felsic eruptions at Pantelleria, the so-called Fastuca eruption was the most powerful of the whole post-caldera period (Orsi *et al.*, 1989) and the related pumice fall can be traced up to 3 km eastwards from the inferred eruptive vent (Rotolo *et al.*, 2007).

Recent studies have highlighted that, although not forming as a whole a homogeneous geochemical clan, the pantellerites at Pantelleria do display distinct geochemical and petrological trends (e.g. Civetta *et al.*, 1998; Avanzinelli *et al.*, 2004; White *et al.*, 2005, 2009). In particular, geochemical and petrological evidence led White *et al.* (2005) to separate pantellerite rocks into five categories, each typified by different phenocryst assemblages, melt peralkalinity index, oxygen fugacity (fO_2) and temperature: these workers noted that (1) fayalite occurrence is limited to melts with PI $< 1{\cdot}6$ and temperatures ≥ 750°C; (2) aenigmatite occurs in rocks with melt PI $> 1{\cdot}5$, whereas aegirine–augite and quartz occur at high PI ($> 1{\cdot}7$) but at low temperature (≤ 700°C). These observations point to an overall low-temperature context (< 800°C) for the petrogenesis of pantellerites, which sharply contrasts with the higher temperatures traditionally advocated for this class of alkali-rich felsic rocks (e.g. Bailey & Macdonald, 1987).

Two contrasting models have been proposed for the petrogenesis of peralkaline magmas at Pantelleria: (1) protracted fractional crystallization from an alkali basalt parental magma (Civetta *et al.*, 1998; White *et al.*, 2009), or (2) a two-step process that involves the low-degree partial melting of alkali gabbroic cumulates to form trachyte melts, which then produce pantellerites by low-pressure fractional crystallization (Lowenstern & Mahood, 1991; Avanzinelli *et al.*, 2004). It is worth stressing that early models (e.g. Civetta *et al.*, 1984; Lowenstern & Mahood, 1991) relied predominantly on geochemical arguments. They did not consider the physical conditions under which magmatic differentiation occurs, such as the temperature of crystal–melt equilibration, or the melt viscosity

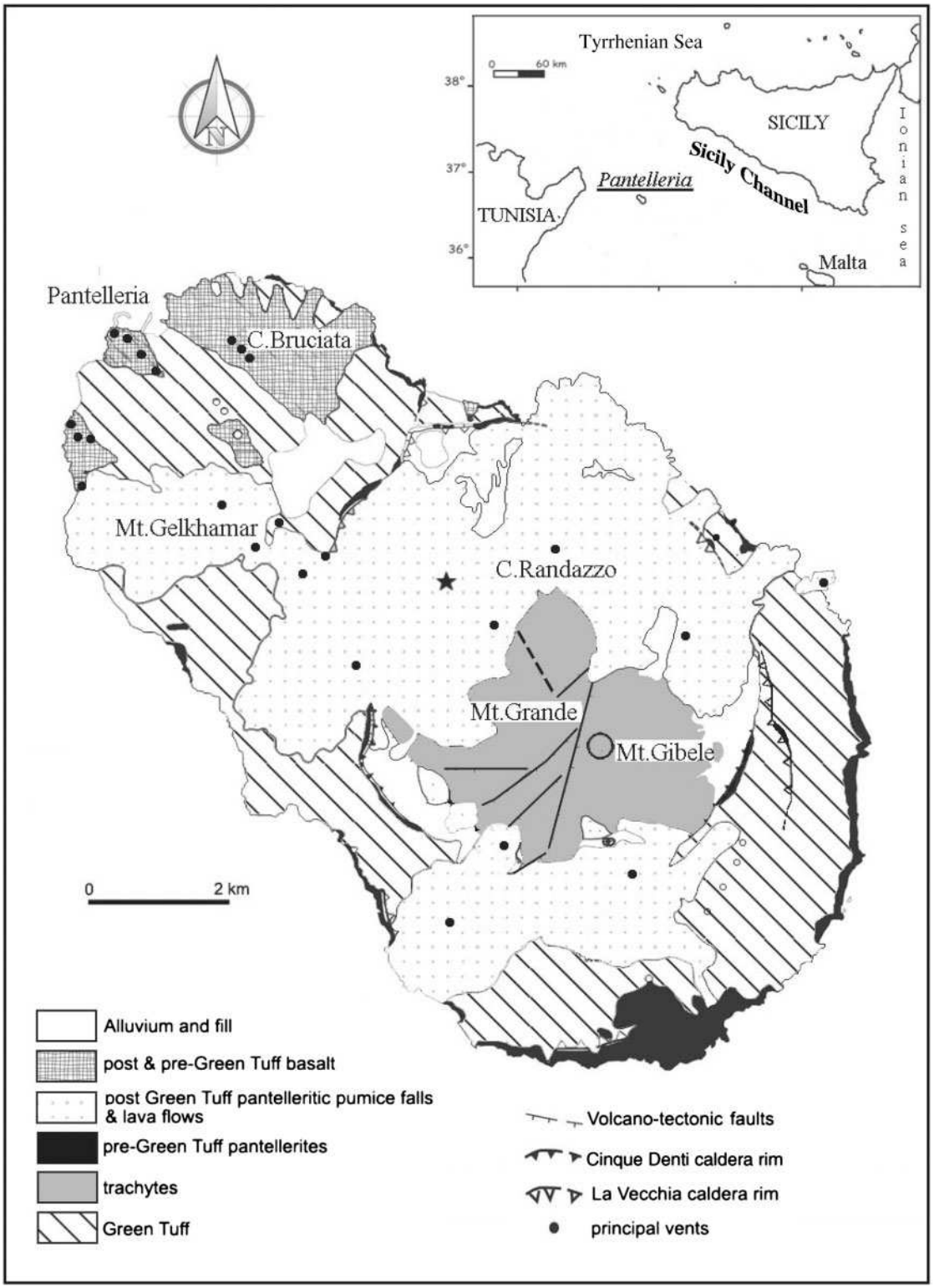

Fig. 1. Structural–tectonic sketch map of Pantelleria island (modified from Rotolo *et al.*, 2007). The star marks the sampling site of the starting material for the experiments.

and density, which heavily depend on temperature and volatile contents. This gap has been partly filled with the detailed petrological studies of White *et al.* (2005, 2009), who used thermobarometric tools (e.g. QUILF) and the MELTS solution model to work out the intensive parameters for the Pantelleria magmatic suite. These studies have confirmed the reduced character of the felsic end-member, significantly below NNO, the low temperatures of crystal–melt equilibrium recorded in the felsic reservoir as stressed above, and the need for extreme fractionation from a mafic parental magma to produce pantellerites. However, despite these advances, there are still considerable uncertainties in the key parameters controlling magma dynamics, such as the pressure of magma storage in the upper crust and the pre-eruptive melt water content. Some insight has been gained into pre-eruptive volatile contents via melt inclusion studies (Kovalenko *et al.*, 1988; Lowenstern & Mahood, 1991; Métrich *et al.*, 2006; Gioncada & Landi, 2010), which concluded that the silicic (rhyolite) melt had several weight per cent H_2O dissolved prior to eruption. However, these estimates still await experimental evaluation, in particular their compatibility with the phenocryst assemblage of the erupted magmas, including the type, composition and proportions of phases. Thermodynamic models such as MELTS have been shown to be of great value in modelling the early stages of magmatic differentiation (from basalt to trachyte) but are still unable to constrain vital petrogenetic attributes of peralkaline felsic magmas, in particular their temperature of last equilibration (see White *et al.*, 2009).

Within this context, our aim in this study is to provide first-order constraints on the role of various intensive parameters in determining crystal–liquid equilibria in rhyolite magmas at Pantelleria (pressure, temperature, H_2O_{melt}) using an experimental approach. Our results provide the basis for future modelling studies, including the numerical simulation of magma ascent and accompanying volatile outgassing (e.g. Papale *et al.*, 1998).

EXPERIMENTAL STRATEGY AND STARTING MATERIAL

A number of studies have demonstrated that peralkaline rhyolitic melts may have high pre-eruptive H_2O contents (up to 6 wt %; Kovalenko *et al.*, 1988; Lowenstern & Mahood, 1991; Webster *et al.*, 1993; Wilding *et al.*, 1993; Barclay *et al.*, 1996; Gioncada & Landi, 2010). Phase equilibria have been constrained at various pressures and temperatures over a range of H_2O_{melt}, from nominally dry to H_2O-saturated conditions (*c.* 6 wt % H_2O at 150 MPa). The explored pressure range (25–150 MPa) reflects the low pressure of storage generally inferred for this category of magmas (Mahood, 1984; Scaillet & Macdonald, 2001), and the geophysical constraints on Pantelleria (e.g. Mattia *et al.*, 2007). The range of temperature investigated (680–800°C) encompasses that inferred by White *et al.* (2005) for the felsic end-members, but also reflects the conditions required to match the crystal-poor condition characterizing most Pantelleria rhyolites, including the selected starting material, and the variation of this parameter with H_2O_{melt}.

The starting material (PAN 01113) belongs to the Fastuca pumice fall eruptive unit (Orsi *et al.*, 1989) and was sampled from the bottom portion of the deposit, which consists of dense, variably welded, pumice that has locally agglutinated to produce vitrophyric bands. Welding and agglutination to form thin, lava-like layers is common at Pantelleria in pumice-fall deposits located close to the vents (Rotolo *et al.*, 2007). PAN 01113 is a pantellerite with PI = 1·4 and a silica content of 70·4 wt % (Table 1). As in all pantellerites, the Al_2O_3 content is low (10·3 wt %) and FeO_{tot} relatively high (7·52 wt %). High field strength elements are considerably enriched in these pantellerite rocks (e.g. Zr = 1876 ppm, Nb = 412 ppm), whereas depletions of Sr (9 ppm) and Ba (151 ppm), suggest an important role for feldspar fractionation during magmatic differentiation.

The phenocryst abundanc in PAN01113 determined by point counting (3009 points), is close to 20 vol. % (vesicle-free), and includes, in order of decreasing abundance, alkali feldspar (15 vol. %), aenigmatite (2·3 vol. %), hedenbergite (1·6 vol. %) and quartz (0·1 vol. %). Amphibole and aegirine microlites (length < 50 μm) occur in trace amounts. Ilmenite microphenocrysts occur in feldspar glomerocrystic clots. Rare microphenocrysts of rounded fayalite (Fa_{93}) are also present.

Both alkali feldspar phenocrysts and microlites have homogeneous compositions ($Ab_{63}Or_{36}$, Table 1). They are euhedral to subhedral with a maximum length of 3 mm, and have a tendency to form glomerocrystic clots. Clinopyroxene mostly occurs as euhedral microphenocrysts (maximum length 0·5 mm) and compositionally is a hedenbergite ($Wo_{43}Fs_{53}$), with a very weak core to rim zonation in CaO (cores being richer, by up to 0·7 wt %, relative to rims). It rarely encloses feldspar microphenocrysts. The occurrence of clinopyroxene within both feldspar and aenigmatite phenocrysts suggests its early appearance in the crystallization sequence. The rare microlites of aegirine possibly represent the last increment of magma crystallization on its way up to the surface (Table 1). Amphibole composition varies within the ferrorichterite–arfvedsonite groups (Na–Fe-rich). Aenigmatite (or cossyrite, named from Cossyra, the ancient name of Pantelleria island) occurs either as euhedral elongate phenocrysts (up to 2 mm in length) or as microphenocrysts (up to 200 μm in length), and does not show significant compositional variations [$X\mathrm{Ti} = \mathrm{Ti}/(\mathrm{Ti} + \mathrm{Fe_{tot}}) = 0{\cdot}16$–$0{\cdot}17$].

Table 1: Composition of PAN 01113 starting glass, groundmass glass, phenocrysts and microphenocrysts in the starting rock

	St. gl. ($n=44$)	gdmss	K-fsp	Ca-cpx	Na-cpx	aenig	amph
SiO_2	70·40(42)	71·5	65·0	47·2	52·9	40·5	49·2
TiO_2	0·48(3)	0·45	0·00	0·73	0·22	9·00	1·77
Al_2O_3	10·30(24)	9·62	18·45	0·42	0·77	0·52	0·65
FeO*	7·52(26)	8·33	1·05	27·7	32·3	40·5	34·2
MnO	0·26(1)	0·00	0·00	1·42	0·84	1·22	1·16
MgO	0·06(1)	0·06	0·00	1·33	0·08	0·40	0·89
CaO	0·52(4)	0·31	0·00	17·9	1·36	0·52	3·30
Na_2O	5·67(30)	6·20	7·42	1·77	11·21	7·11	7·32
K_2O	4·74(9)	4·42	6·19	0·00	0·16	0·01	1·48
Total	100·0	100·9	98·1	98·5	99·8	99·8	100·0
Sr (ppm)	9						
Zr	1876						
Nb	412						
Ba	151						

St. gl., starting glass (one standard deviation in terms of last digit given in parentheses); gdmss, groundmass; k-fsp, alkali feldspar; Ca-cpx, Ca-rich clinopyroxene (microphenocrysts); Na-Cpx, Na-rich clinopyroxene (microlite); aenig, aenigmatite; amph, amphibole (microlite). *n*, number of electron microprobe analyses of starting glass.

EXPERIMENTAL METHODS

The starting rock sample was first powdered and then fused twice at 1200°C in a Pt crucible for 4 h in air. The resulting glass was analyzed by electron microprobe to check its composition; a small Na loss was detected compared with the whole-rock X-ray fluorescence analysis (Table 1). The glass was then ground to a powder of 10–40 μm grain size and used as the starting material: this technique avoids the persistence of phenocrysts or microlites during crystallization experiments, and renders more straightforward the interpretation of the experimental results (see Pichavant *et al.*, 2007). About 30 mg of powder was loaded in Au capsules (1·5 cm in length, inner diameter 2·5 mm, outer diameter 2·9 mm). Prior to the sample powder, distilled water and CO_2 (added as silver oxalate) were loaded at the bottom of each capsule, varying the XH_2O_{loaded} [$=$ moles of $H_2O/(H_2O+CO_2)$] in the range 0–1 (i.e. from pure CO_2 to pure H_2O; Table 2). The capsules were then welded shut while kept within a liquid nitrogen bath so as to prevent water loss, and then reweighed.

Experiments were conducted in an internally heated pressure vessel (IHPV), working vertically and equipped with a double wound Kanthal furnace. The pressurizing medium was a mixture of Ar and H_2, whose Ar/H_2 ratio was fixed by sequential loading at room temperature, so as to reach the desired target fO_2 (Scaillet *et al.*, 1992). Pressure was recorded by a transducer calibrated against a Heise–Bourdon tube gauge (uncertainty ± 20 bars). Three chromel–alumel thermocouples allowed the continuous control of temperature over the hotspot length (4 cm). Uncertainties in temperature are estimated to be ± 5°C. Redox conditions were mostly in the range NNO − 1 to NNO − 2 (for charges at, or close to, H_2O saturation; see below and Table 2) and checked by the use of an H_2 membrane (Schmidt *et al.*, 1995) for some experiments at 150 MPa (750 and 800°C, runs 2 and 3; see Table 2).

The determination of fO_2 specific to each charge was made in the following ways. For H_2O-saturated charges fO_2 was calculated from the dissociation equilibrium of water, using the equilibrium constant, K_w [$= fH_2O/(fH_2 \times fO_2^{1/2})$], from Robie *et al.* (1979), fH_2O of pure water at the T and P of interest from Burnham *et al.* (1969), and fH_2 as given by the membrane when used. In runs where the H_2 membrane could not be used, the prevailing fH_2 of a given experiment was calculated using an empirical factor between the partial H_2 pressure loaded at room temperature and that reached once the vessel was equilibrated at P and T. Experiments made with H_2 membranes over several years show that, for a given run, such an empirical factor for the IHPV vessel used in this study is 3 ± 1 (i.e. the final fH_2 is 3 ± 1 times higher than that applied at room temperature), depending in large part on the fH_2 of the previous run (i.e. the H_2 memory of the vessel). The reported values of fH_2 in Table 2 correspond to those obtained by multiplying the room temperature hydrogen pressure by a factor of three. Although such an approach yields an fO_2 with a greater uncertainty than when using an

Table 2: Experimental conditions and run products

Charge	H_2O[1] (wt %)	fH_2 (MPa)	fH_2O[2] (MPa)	log fO_2	ΔNNO	XH_2O_{in}[3]	H_2O_m[4] (wt %)	Cl_m[5] (wt %)	Phases present and abundances (wt %)	R^2
Run 3, 800°C, 150 MPa, 211 h										
19	6·40	1·1	151·0	−14·12	−0·25	1·00	6·15	0·19	gl(99) + Ti-mt(1)	0·17
18	4·30	1·1	109·1	−14·40	−0·53	1·00	4·87	0·22	gl(99) + Ti-mt(1)	0·08
17	3·00	1·1	89·1	−14·58	−0·71	1·00	4·21	0·25	gl(99) + Ti-mt(1)	0·11
16	2·10	1·1	77·0	−14·71	−0·83	1·00	3·79	0·27	gl(99) + Ti-mt(1)	0·64
15	1·00	1·1	21·8	−15·80	−1·93	1·00	1·53	0·29	gl(99) + cpx(1)	0·67
14	0·70	1·1	14·2	−16·18	−2·30	1·00	1·12	0·32	gl(87) + cpx(2) + K-fsp(11)	0·18
13	0·00	1·1	0·1	≤ -19	≤-3	1·00	≤1·12	0·36	gl(79) + cpx(tr) + K-fsp(23)	0·84
Run 2, 750°C, 150 MPa, 288 h										
12	6·10	1·3	124·6	−15·57	−0·58	1·00	5·36	0·33	gl(96) + cpx(1) + Ti-mt(2)	1·30
11	4·30	1·3	135·0	−15·50	-0·51	1·00	5·68	0·37	gl(97) + cpx(2) + Ti-mt(2)	1·27
10	3·00	1·3	113·7	−15·65	−0·66	1·00	5·02	0·39	gl(97) + cpx(2) + Ti-mt(2)	1·28
9	2·00	1·3	104·1	−15·73	−0·74	1·00	4·71	0·44	gl(97) + cpx(2) + Ti-mt(2)	1·13
8	1·10	1·3	24·8	−16·97	−1·99	1·00	1·68	0·50	gl(88) + cpx(4) + K-fsp(7) + Ti-mt(1) + ilm(tr)	0·08
7	0·60	1·3	4·9	−18·33	−3·40	1·00	0·52	0·57	gl(72) + cpx(6) + K-fsp(22)	0·27
6	0·00	1·3	4·6	−18·44	−3·45	1·00	0·50	0·78	gl(38) + K-fsp(40) + aenig(9) + qz(13)	0·90
Run 4, 725°C, 150 MPa, 360 h										
1	3·00	2·0	131·4	−16·51	−0·92	1·00	5·57	0·39	gl(97) + cpx(2) + Ti-mt(1)	1·50
2	2·30	2·0	100·7	−16·74	−1·15	0·89	4·60	0·45	gl(97) + cpx(2) + Ti-mt(1)	0·84
4	1·40	2·0	47·1	−17·40	−1·81	0·64	2·66	0·52	gl(84) + cpx(4) + K-fsp(10) + aenig(2)	0·24
5	1·00	2·0	64·8	−17·12	−1·54	0·51	3·35	0·47	gl(64) + cpx(5) + K-fsp(28) + aenig(3)	0·33
6	0·70	2·0	48·5	−17·37	−1·79	0·38	2·72	0·50	gl(75) + cpx(3) + K-fsp(20) + aenig(3)	0·29
7	0·00	2·0	6·6	−19·11	−3·53	0·00	0·65	0·83	gl(46) + cpx(7) + K-fsp(44) + aenig(tr) + qz(3)	0·06
Run 9, 680°C, 150 MPa, 333 h										
1	3·40	2·1	116·0	−17·80	−1·06	1·00	5·09	0·24	gl(77) + K-fsp + amph + Ti-mt	n.d.
2	2·40	2·1	101·1	−17·92	−1·17	0·91	4·61	0·35	gl(49) + cpx + amph + K-fsp + aenig	n.d.
3	1·30	2·1	73·9	−18·19	−1·45	0·72	3·68	0·43	gl + amph + K-fsp + aenig + qz	n.d.
4	1·50	2·1	71·9	−18·22	−1·47	0·71	3·61	0·26	gl + cpx + amph + K-fsp + aenig + qz	n.d.
5	1·10	2·1	56·0	−18·43	−1·69	0·59	3·01	n.d.	gl + cpx + amph + K-fsp + aenig + qz	n.d.
6	0·70	2·1	36·4	−18·81	−2·06	0·43	2·21	n.d.	gl + cpx + amph + K-fsp + aenig + qz	n.d.
7	0·00	2·1	4·6	−20·60	−3·86	0·00	≤2·21	n.d.	gl(3) + cpx(tr) + amph(21) + Kfsp(62) + qz(14)	0·43
Run 8, 800°C, 100 MPa, 147 h										
1	3·10	2·3	83·0	−15·25	−1·37	1·00	4·00	0·27	gl(99) + Ti-mt(1)	2·61
2	2·20	2·3	46·4	−15·76	−1·87	0·87	2·63	0·26	gl(92) + cpx(8)	4·17
3	1·90	2·3	62·9	−15·50	−1·61	0·77	3·28	0·29	gl(96) + cpx(4)	1·33
4	1·50	2·3	28·5	−16·18	−2·30	0·66	1·85	0·30	gl(96) + cpx(4)	0·7
5	1·20	2·3	28·4	−16·19	−2·30	0·55	1·85	0·30	gl(86) + cpx(3) + K-fsp(11)	0·28
6	0·80	2·3	16·2	−16·68	−2·79	0·42	1·23	0·30	gl(78) + cpx(7) + k-fsp(15)	0·91
7	0·00	2·3	14·2	−16·79	−2·90	0·00	1·13	0·37	gl(70) + cpx(3) + K-fsp(26) + qz(1)	1·09
Run 11, 680°C, 100 MPa, 476 h										
1	3·30	2·4	86·1	−18·17	−1·42	1·00	4·11	0·41	gl(64) + K-fsp(26) + cpx(4) + aenig(7)	0·69
2	1·90	2·4	61·1	−18·47	−1·72	0·78	3·21	n.d.	gl + K-fsp + cpx + aenig + amph + qz	n.d.
3	1·20	2·4	41·5	−18·81	−2·05	0·59	2·43	n.d.	gl + K-fsp + cpx + amph + qz	n.d.
Run 5, 800°C, 50 MPa, 286 h										
1	2·20	2·1	48·5	−15·66	−1·77	1·00	2·72	0·56	gl(99) + cpx(1)	0·19
2	1·80	2·1	37·5	−15·89	−1·99	0·83	2·26	0·53	gl(99) + cpx(1)	0·28
3	1·60	2·1	33·3	−15·99	−2·09	0·76	2·07	0·57	gl(98) + K-fsp(2) + cpx(tr)	0·35
4	1·40	2·1	29·0	−16·11	−2·21	0·69	1·88	0·62	gl(83) + cpx(3) + K-fsp(14)	0·29
5	1·20	2·1	24·8	−16·25	−2·35	0·62	1·68	0·64	gl(84) + K-fsp(16) + cpx(tr) + qz(tr)	0·16

(continued)

Table 2: Continued

Charge	H_2O[1] (wt %)	fH_2 (MPa)	fH_2O[2] (MPa)	log fO_2	ΔNNO	XH_2O_{in}[3]	H_2O_m[4] (wt %)	Cl_m[5] (wt %)	Phases present and abundances (wt %)	R^2
Run 5, 800°C, 50 MPa, 286 h										
6	1·10	2·1	20·3	−16·42	−2·52	0·53	1·45	0·62	gl(78) + cpx(2) + K-fsp(20)	0·17
7	0·00	2·1	0·1	−16·87	−2·97	0·00	1·00	1·01	gl(37) + K-fsp(46) + qz(15) + fe°(2)	0·60
Run 6, 750°C, 50 MPa, 308 h										
1	2·20	2·1	25·9	−17·35	−2·34	1·00	1·73	0·54	gl(79) + cpx(10) + K-fsp(11)	0·42
2	1·90	2·1	28·0	−17·29	−2·28	0·87	1·83	0·59	gl(72) + cpx(6) + K-fsp(22)	0·28
3	1·80	2·1	14·0	−17·89	−2·88	0·80	1·11	0·62	gl(70) + cpx(5) + K-fsp(25) + ilm(tr)	0·32
4	1·10	2·1	18·3	−17·65	−2·64	0·61	1·35	0·70	gl(64) + cpx(3) + K-fsp(33) + qz(tr)	0·19
5	0·90	2·1	7·8	−18·40	−3·38	0·52	0·73	0·75	gl(68) + cpx(3) + K-fsp(29)	0·29
6	0·60	2·1	9·2	−18·25	−3·24	0·41	0·82	0·76	gl(62) + cpx(3) + K-fsp(33) + qz(2)	0·19
7	0·00	2·1	4·1	−18·95	−3·94	0·00	0·46	1·09	gl(30) + cpx(5) + Kfsp(48) + qz(12) + aenig(5)	0·51
Run 10, 680°C, 50 MPa, 500 h										
1	3·10	1·8	45·8	−18·47	−1·70	1·00	2·61	n.d.	gl + K-fsp + qz + cpx + amph + ilm	n.d.
2	2·00	1·8	32·6	−18·77	−2·00	0·78	2·04	n.d.	gl + K-fsp + qz + cpx + amph + ilm	n.d.
3	1·30	1·8	22·7	−19·08	−2·31	0·60	1·58	n.d.	gl + K-fsp + qz + cpx + amph + ilm	n.d.
4	0·80	1·8	14·0	−19·50	−2·73	0·43	1·11	n.d.	gl + K-fsp + qz + cpx + amph + ilm	n.d.
Run 7, 800°C, 25 MPa, 298 h										
1	1·10	1·5	24·3	−15·97	−2·07	1·00	1·65	0·32	gl(81) + cpx(4) + K-fsp(15)	0·38
2	1·00	1·5	7·1	−17·04	−3·14	0·89	0·68	0·36	gl(78) + cpx(6) + K-fsp(16)	0·58
3	0·50	1·5	18·4	−16·21	−2·31	0·73	1·36	0·35	gl(68) + cpx(7) + K-fsp(25)	0·74
4	0·40	1·5	23·1	−16·01	−2·11	0·61	1·59	0·32	gl(66) + cpx(6) + K-fsp(28)	0·98
5	0·30	1·5	7·8	−16·96	−3·06	0·54	0·73	0·38	gl(62) + cpx(3) + K-fsp(35) + qz(tr)	0·51
6	0·50	1·5	3·5	−17·66	−3·76	0·63	0·41	0·35	gl(69) + cpx(4) + K-fsp(27)	0·92
7	0·00	1·5	7·9	−16·95	−3·05	0·00	0·74	0·40	gl(68) + cpx(3) + K-fsp(29) + qz(tr)	0·61

[1]Bulk H_2O content of the charge.
[2]H_2O fugacity calculated using the amount of dissolved H_2O in glass, with the expression $fH_2O = 12{\cdot}084(H_2O_{melt})^{1{\cdot}39}$ as explained in the text. $\Delta NNO = \log fO_2 - \log fO_2$ of the NNO buffer calculated at P and T (Pownceby & O'Neill, 1994; O'Neill & Pownceby, 1993).
[3]Initial mole fraction of H_2O of the C–O–H fluid loaded to the capsule.
[4]Dissolved H_2O in the glass determined using the by-difference method. (See text for explanation.)
[5]Amount of Cl dissolved in the glass determined by EPMA.
Phase abbreviations: gl, glass; k-fsp, K-feldspar; qz, quartz; cpx, clinopyroxene; aenig, aenigmatite; amph, amphibole, ti-mt, ti-magnetite; ilm, ilmenite.

H_2 membrane, under the moderately reduced conditions explored in this study, variations in fH_2 arising from the use of a factor of two or four affect the calculated fO_2 by either + 0·4 (factor of two) or −0·3 (factor of four) log units relative to that obtained with a factor of three. For H_2O-undersaturated charges, the same procedure as above was used except for fH_2O which was estimated following Scaillet & Macdonald (2006): we used an empirical relationship of the form $fH_2O = a(H_2O_{melt})^b$, to calculate the prevailing fH_2O from H_2O_{melt} obtained as explained below. The coefficients were derived from water-saturated experiments conducted on PAN 01113 rhyolite (Di Carlo *et al.*, in preparation), and found to be $a = 12{\cdot}084$ and $b = 1{\cdot}39$ (with H_2O_{melt} in wt %, to retrieve fH_2O in MPa).

The calculated fO_2 values of H_2O-saturated charges cluster around NNO − 2 (Table 2), each run showing a range in fO_2, from NNO − 3 up to NNO, which reflects the variation in melt water content (and thus fH_2O) achieved within a single run between different charges, the lowest fO_2 being those of the water-poorer charges. Only extremely dry charges (i.e. having close to zero dissolved H_2O_{melt}) depart significantly from the above clustering, reaching fO_2 as low as NNO − 4 (Table 2). However, the calculated fO_2 for those near-anhydrous charges is extremely sensitive to small changes of H_2O_{melt} (see Webster *et al.*, 1987) and thus such fO_2 values should be considered with caution. At this point we stress that the conclusions of our study are based mainly on results from near-liquidus, or water-rich, charges for which a

good control of redox conditions could be afforded. Therefore, excluding the dry outliers, the typical uncertainty on fO_2 is less than $\pm 0{\cdot}1$ for runs performed with an H_2-membrane, and rises to $\pm 0{\cdot}4$ log units for the others (e.g. Scaillet *et al.*, 1995; Martel *et al.*, 1999; Scaillet & Evans, 1999; Costa *et al.*, 2004).

Runs were terminated by switching off the power supply and cooling the vessel in a vertical position. Quench crystals were never observed. Run duration varied between 147 and 500 h; the lower the temperature the longer the run duration. After each experiment the capsules were weighted to check for leaks and opened. For each charge one half of the run product was mounted in epoxy and polished. A total number of 56 phase equilibrium experiments were performed.

ANALYTICAL TECHNIQUES

Run products were first observed by scanning electron microscopy–energy-dispersive spectrometry (SEM–EDS; Cambridge LEO 440, at the University of Palermo and a JEOL WINSET JSM 6400, at ISTO, Orléans), for preliminary phase identification and textural analysis. Experimental glasses, minerals and solid sensors were then analysed by electron microprobe (EMP), using either a Cameca Camebax or a Cameca SX50, both at the joint BRGM–CNRS–University of Orléans analytical facility, Orléans. Analytical conditions were an accelerating voltage of 15 kV, sample current of 6 nA, and counting time of 10 s on peak and background for all the elements; Na and K were analysed first and a ZAF correction was applied. A focused beam was used for mineral phases and a defocused one (*c.* 5–8 μm) for glasses. The chlorine content of glasses was measured using a counting time of 60 s for both peak and background. The by-difference method (Devine *et al.*, 1995) was used to estimate the H_2O content of glasses of crystal-rich charges, after correction for alkali migration. Four pantellerite experimental glasses, with well-known H_2O contents, were used as secondary standards to calibrate the method. The accuracy of this method for H_2O_{melt} is thought to be $\pm 0{\cdot}5$ wt % at best; for charges analysed during the same session, the precision in H_2O_{melt} is estimated to be $\pm 0{\cdot}3$ wt %. The pantellerite glass standards were also used to calibrate the correction factor for the migration of Na. Where the by-difference method was unsuccessful (e.g. in all low-T crystal-rich charges in which glass analyses were either impossible or yielded meaningless results in terms of H_2O_{melt}) the following relationships was used to calculate the H_2O_{melt} (Scaillet & Macdonald, 2006):

$$H_2O \text{ wt } \% = H_2O_{sat} \times XH_2O_{fluid}$$

where XH_2O_{fluid} is the mole fraction of fluid loaded in the capsule ($= XH_2O_{loaded}$; see above) and H_2O_{sat} is the melt water content at saturation at the relevant pressure. In a few crystal-poor charges (numbers 5-2, 8-2, 8-3 and 8-4) the amounts of dissolved H_2O and CO_2 were analysed by Fourier transform infra-red (FTIR) spectroscopy; CO_2 was found to be always below the detection limit (i.e. <50 ppm).

Phase proportions for each charge were computed by mass-balance calculations (Albarède, 1995), using all major element oxides on an anhydrous basis. As a rule, we considered reliable phase proportions yielding squared residuals <1; charges with the sum of squared residuals exceeding unity are interpreted as primarily reflecting an underestimation of the correction factor for Na electron microprobe analysis in glass.

ATTAINMENT OF EQUILIBRIUM AND IRON LOSS

All experiments from this study are of crystallization-type, and follow the procedures used by Scaillet & Macdonald (2001, 2006) on similar compositions (see Pichavant *et al.*, 2007, for a detailed discussion). In particular, the run duration of the experiments (300 h on average) proved to be long enough to ensure close attainment of crystal–melt equilibrium, based on the following lines of evidence: (1) euhedral crystals that are evenly distributed across the charge; (2) mass-balance calculations that yielded low squared residuals for the vast majority of charges, demonstrating that the analysed phases are homogeneous within analytical uncertainty; (3) the general internal coherency of compositional trends (i.e. the variation of phase compositions vs experimental variables). As discussed below, in heavily crystallized charges, calculated phase proportions agree well with expected modal abundances of feldspar and quartz in fully crystallized silicic rocks rich in iron (i.e. peralkaline granites), therefore stressing that our study encountered no particular problem in growing the major phases in cotectic proportions even under conditions usually considered as kinetically unfavourable to the attainment of equilibrium (i.e. close to the solidus, which implies either low temperature or low water content, or both). In all cases, iron loss from the experimental charge to the noble metal of the capsule was less than 3% relative to the bulk Fe content of the starting material, owing to the use of Au capsules.

EXPERIMENTAL RESULTS

The experimental conditions and phase proportions are listed in Table 2, and Table 3 reports phase compositions. The mineral phases identified by SEM–EDS were alkali feldspar, pyroxene, quartz, amphibole, aenigmatite, ilmenite and Ti-magnetite. Aenigmatite, pyroxene, amphibole and quartz are always well faceted, with a length in the range 10–30 μm, the greater size being achieved in low-temperature–low-H_2O_{melt} charges. Owing to their small size and elongated shape, most clinopyroxene analyses

Table 3: Compositions of the experimental phases

Run-charge	Phase	SiO_2	TiO_2	Al_2O_3	FeO	MnO	MgO	CaO	Na_2O	K_2O	Total	Mole fractions
3-13	gl[1](7)[2]	70·30(22)[3]	0·75(9)	8·11(68)	8·93(56)	0·37(9)	0·09(3)	0·59(9)	6·38(20)	4·51(25)	96·70	
	K-fsp(4)	67·35(66)	0·19(9)	14·52(84)	3·20(49)	0·14(9)	0·03(1)	0·14(6)	7·02(26)	5·30(11)	97·90	$Ab_{67}Or_{32}$
	cpx	n.d.										
3-14	gl(8)	70·90(32)	0·60(6)	9·40(16)	7·71(26)	0·28(14)	0·06(4)	0·46(7)	5·94(9)	4·63(13)	94·50	
	K-fsp(1)	65·16	0·13	14·98	3·57	0·08	0·02	0·24	7·06	5·26	96·52	$Ab_{66}Or_{32}$
	cpx(2)	47·66(20)	0·45(13)	0·24(2)	27·59(6)	1·20(7)	1·95(13)	16·62(100)	2·68(101)		98·41	$XFe_{tot} = 0·89$
3-15	gl(7)	70·40(24)	0·57(5)	10·30(7)	7·45(26)	0·30(9)	0·07(2)	0·53(5)	5·80(17)	4·67(7)	94·00	
	cpx(2)	48·61(38)	0·54(7)	0·09(11)	26·11(66)	1·37(2)	2·36(1)	17·41(10)	2·68(32)		99·17	$XFe_{tot} = 0·86$
3-16	gl(7)	70·90(49)	0·58(3)	10·20(11)	7·41(26)	0·32(9)	0·08(3)	0·61(6)	5·35(16)	4·60(7)	91·40	
	Ti-mt(2)	0·26(1)	14·05(0)	0·17(5)	78·19(31)	1·26(9)	0·15(2)	0·02(2)	0·01(1)	0·11(1)	94·22	
3-17	gl(7)	70·50(42)	0·54(8)	10·30(14)	7·35(36)	0·22(9)	0·08(3)	0·54(9)	5·91(18)	4·57(10)	90·90	
	Ti-mt(2)	0·77(42)	13·83(9)	0·21(2)	79·04(97)	1·24(0)	0·13(1)	0·05(1)	0·21(4)	0·11(7)	95·59	
3-18	gl(7)	70·50(46)	0·53(5)	10·20(13)	7·31(29)	0·24(8)	0·09(4)	0·54(4)	5·92(20)	4·61(9)	90·20	
	Ti-mt(3)	0·22(6)	13·86(15)	0·15(4)	80·18(101)	1·32(6)	0·16(7)	0·01(2)	0·02(2)	0·07(4)	95·99	
3-19	gl(5)	70·70(39)	0·49(5)	10·20(8)	7·32(15)	0·29(12)	0·09(2)	0·61(6)	5·86(19)	4·44(14)	88·70	
	Ti-mt	n.d.										
2-6	gl(4)	68·30(26)	0·52(10)	9·78(83)	7·80(98)	0·27(6)	0·06(2)	0·43(7)	7·63(24)	5·18(14)	97·00	
	K-fsp(7)	67·32(87)	0·06(4)	15·02(90)	2·82(53)	0·08(13)	0·01(1)	0·05(6)	6·90(16)	6·11(15)	98·37	$Ab_{63}Or_{37}$
	Aenig(8)	45·96(124)	7·86(37)	1·62(76)	36·09(194)	1·19(20)	0·49(5)	0·44(46)	7·17(19)	0·67(35)	101·48	$XTi = 0·16$
2-7	gl(8)	72·30(40)	0·49(5)	9·18(89)	7·15(81)	0·30(5)	0·05(2)	0·26(7)	5·69(24)	4·61(28)	94·90	
	K-fsp(7)	67·52(84)	0·16(8)	14·86(98)	3·45(59)	0·05(6)	0·01(1)	0·10(13)	6·97(45)	5·35(30)	98·47	$Ab_{66}Or_{33}$
	cpx(6)	49·56(96)	0·95(17)	0·01(78)	29·02(127)	1·33(19)	1·32(16)	12·17(88)	4·92(92)		99·27	$XFe_{tot} = 0·93$
2-8	gl(8)	71·40(31)	0·48(9)	10·10(54)	7·14(48)	0·26(11)	0·04(2)	0·20(5)	5·71(29)	4·67(12)	93·60	
	K-fsp(1)	65·85	0·09	17·35	2·40	0·00	0·21	0·17	7·93	5·99	99·99	$Ab_{66}Or_{33}$
	cpx(2)	51·27(49)	0·38(51)	1·57(37)	25·12(10)	1·36(28)	1·35(15)	12·31(60)	4·91(50)		98·27	$XFe_{tot} = 0·91$
	ilm(1)	1·04	50·72	0·31	43·55	2·25	0·37	0·54	0·12	0·49	99·39	
	Ti-mt	n.d.										
2-9	gl(6)	72·20(34)	0·40(5)	10·40(14)	6·49(32)	0·23(12)	0·06(3)	0·34(9)	5·26(15)	4·62(15)	90·10	
	cpx(4)	49·30(37)	0·44(18)	0·22(16)	26·10(27)	1·46(14)	2·15(12)	16·46(117)	3·31(75)		99·46	$XFe_{tot} = 0·87$
	Ti-mt	n.d.										
2-10	gl(8)	72·00(33)	0·47(7)	10·40(22)	6·71(29)	0·22(7)	0·05(3)	0·29(5)	5·17(19)	4·64(12)	89·80	
	cpx(4)	49·29(135)	0·49(8)	0·36(101)	26·10(131)	1·37(29)	2·17(20)	16·46(168)	3·24(24)		99·13	$XFe_{tot} = 0·87$
	Ti-mt	n.d.										
2-11	gl(8)	72·30(62)	0·41(8)	10·40(17)	6·45(40)	0·24(5)	0·06(2)	0·32(7)	5·18(16)	4·68(15)	89·00	
	cpx(3)	48·75(44)	0·57(5)	0·25(3)	26·07(77)	1·45(9)	2·17(12)	16·50(20)	3·39(11)		99·15	$XFe_{tot} = 0·87$
	Ti-mt	n.d.										
2-12	gl(7)	72·30(52)	0·44(7)	10·50(8)	6·27(27)	0·24(11)	0·05(3)	0·35(4)	5·13(17)	4·71(16)	89·50	
	cpx(2)	48·39(105)	0·44(7)	0·93(90)	24·43(239)	1·73(10)	2·04(11)	16·30(97)	2·37(42)		96·63	$XFe_{tot} = 0·87$
	Ti-mt	n.d.										
4-1	gl(12)	71·80(59)	0·36(7)	10·20(19)	7·18(39)	0·41(16)	0·06(3)	0·29(13)	5·18(31)	4·54(13)	90·20	
	cpx(5)	51·10(125)	0·40(8)	1·22(51)	23·64(97)	1·31(7)	1·84(8)	15·11(79)	5·07(48)		99·70	$XFe_{tot} = 0·89$
	Ti-mt	n.d.										
4-2	gl(11)	71·60(46)	0·34(7)	10·30(15)	7·26(52)	0·21(17)	0·04(4)	0·23(6)	5·45(19)	4·57(21)	91·40	
	cpx(3)	50·84(172)	0·58(9)	0·92(88)	24·73(130)	1·31(17)	1·73(12)	14·69(115)	5·06(11)		99·86	$XFe_{tot} = 0·89$
	Ti-mt	n.d.										
4-4	gl(9)	71·40(22)	0·38(8)	9·78(95)	7·05(86)	0·22(15)	0·03(2)	0·25(5)	6·27(28)	4·60(35)	93·70	
	K-fsp(3)	67·08(24)	0·14(9)	16·14(117)	3·03(149)	0·09(3)	0·17(4)	0·20(23)	7·36(19)	5·62(28)	99·83	$Ab_{66}Or_{33}$

(continued)

Table 3: Continued

Run-charge	Phase	SiO_2	TiO_2	Al_2O_3	FeO	MnO	MgO	CaO	Na_2O	K_2O	Total	Mole fractions
	cpx(1)	51·03	0·89	1·15	26·72	1·13	1·07	12·73	5·46		100·19	$XFe_{tot} = 0·94$
	aenig(1)	41·82	8·74	0·90	38·03	1·34	0·63	0·39	8·18	0·05	100·08	$XTi = 0·17$
4-5	gl(6)	73·10(76)	0·39(7)	8·78(66)	7·50(91)	0·38(7)	0·05(3)	0·28(6)	5·15(98)	4·40(22)	92·90	
	K-fsp(4)	67·34(77)	0·06(11)	16·23(117)	2·88(49)	0·04(2)	0·16(7)	0·09(4)	7·22(40)	5·67(25)	99·69	$Ab_{66}Or_{34}$
	cpx(1)	51·56	0·69	0·81	24·99	1·43	1·10	12·02	6·98		99·58	$XFe_{tot} = 0·93$
	aenig(1)	42·01	8·41	1·35	37·75	1·41	0·65	0·45	7·87	0·25	100·15	$XTi = 0·17$
4-6	gl(5)	71·80(41)	0·52(7)	8·86(90)	7·37(68)	0·45(22)	0·04(3)	0·41(14)	5·96(4)	4·63(31)	93·60	
	K-fsp(2)	67·25(0)	0·11(8)	16·27(33)	2·49(9)	0·10(7)	0·15(1)	0·05(1)	7·56(24)	5·80(7)	99·78	$Ab_{66}Or_{33}$
	cpx(2)	50·75(195)	1·36(6)	0·31(74)	25·69(131)	0·97(9)	1·39(23)	12·57(137)	6·43(20)		99·46	$XFe_{tot} = 0·92$
	aenig(1)	41·66	8·80	0·41	36·97	1·24	0·68	0·24	8·14	0·12	98·25	$XTi = 0·18$
4-7	gl(2)	72·40(53)	0·50(4)	6·22(54)	11·40(67)	0·64(8)	0·15(2)	0·04(3)	4·63(76)	4·02(42)	92·50	
	K-fsp(4)	67·04(39)	0·19(17)	16·05(54)	2·87(85)	0·16(4)	0·17(4)	0·05(6)	7·32(10)	6·11(5)	99·97	$Ab_{64}Or_{35}$
	cpx(1)	43·67	1·28	3·42	26·75	0·94	1·21	13·82	8·95		100·03	$XFe_{tot} = 0·94$
	aenig(1)	42·75	8·47	0·61	37·77	1·16	0·67	0·28	8·36	0·02	100·10	$XTi = 0·17$
9-1	gl(10)	74·72(53)	0·26(5)	10·58(17)	5·26(45)	0·14(10)	0·02(3)	0·09(5)	4·85(20)	4·08(13)	87·20	
	K-fsp(4)	64·77(53)	0·13(6)	17·48(14)	2·59(63)	0·00(0)	0·00(0)	0·26(15)	5·45(23)	9·33(40)	100·00	$Ab_{46}Or_{52}$
	amph(6)	47·45(81)	1·85(16)	1·80(35)	30·20(94)	1·20(11)	1·53(31)	3·75(54)	5·78(20)	1·17(16)	94·73	
	Ti-mt(1)	4·19	10·17	0·59	73·00	1·06	0·04	0·06	0·21	0·26	89·57	
9-2	gl(7)	75·56(38)	0·28(3)	9·51(22)	5·86(24)	0·21(3)	0·02(3)	0·13(7)	4·37(49)	4·07(17)	86·41	
	cpx(1)	53·13	1·27	1·43	25·41	0·88	0·98	6·08	10·00	0·58	99·72	$XFe_{tot} = 0·94$
	amph(2)	48·59(81)	1·43(7)	1·44(47)	30·55(100)	1·32(43)	1·49(94)	2·32(91)	6·18(5)	1·16(19)	94·46	
	K-fsp(5)	65·31(34)	0·09(7)	17·62(49)	2·24(45)	0·01(14)	0·10(7)	0·08(5)	5·81(42)	8·78(54)	100·00	$Ab_{50}Or_{50}$
	aenig(4)	40·91(57)	6·74(43)	1·04(16)	38·37(63)	1·15(28)	0·40(8)	0·45(14)	6·69(18)	0·21(11)	95·97	$XTi = 0·14$
9-3	gl(4)	76·05(57)	0·34(7)	8·35(13)	6·27(22)	0·21(12)	0·01(1)	0·18(14)	4·51(49)	4·10(15)	87·45	
	amph(8)	47·74(63)	1·89(42)	0·84(29)	31·22(65)	1·35(25)	1·48(37)	2·72(19)	6·23(34)	1·00(13)	94·47	
	aenig(1)	40·63	7·96	0·46	38·97	1·56	0·32	0·15	6·61	0·18	96·84	$XTi = 0·16$
	K-fsp(4)	65·97(112)	0·12(4)	16·86(109)	3·06(108)	0·02(8)	0·10(11)	0·04(4)	6·49(12)	7·29(61)	100·00	$Ab_{57}Or_{42}$
9-4	gl(1)	73·61	0·32	8·82	6·54	0·51	0·00	0·15	5·27	4·77	87·90	
	amph(5)	47·87(66)	2·21(30)	0·67(13)	31·25(85)	1·40(15)	1·14(14)	2·30(19)	6·94(29)	1·21(13)	94·98	
	K-fsp(4)	67·19(60)	0·12(12)	15·62(98)	3·41(78)	0·15(5)	0·10(10)	0·09(4)	6·64(36)	6·58(28)	100·00	$Ab_{60}Or_{39}$
	aenig(2)	43·04(69)	7·44(61)	1·18(60)	39·54(123)	1·45(11)	0·26(5)	0·27(1)	8·24(2)	0·32(24)	101·75	$XTi = 0·15$
	cpx(2)	51·09(137)	1·27(8)	1·06(68)	26·59(190)	0·85(1)	0·57(2)	6·66(132)	11·64(71)		99·00	$XFe_{tot} = 0·96$
9-5	gl(4)	72·74(35)	0·51(5)	7·07(9)	8·29(33)	0·49(12)	0·05(2)	0·20(2)	6·54(81)	4·12(17)	88·51	
	amph(3)	48·79(91)	2·35(7)	1·53(74)	28·10(51)	1·31(6)	1·11(17)	1·89(6)	7·03(12)	1·61(26)	93·72	
	K-fsp(2)	65·53(27)	0·01(12)	17·67(12)	2·21(23)	0·00(0)	0·19(11)	0·13(3)	6·76(16)	7·51(4)	100·00	$Ab_{57}Or_{42}$
	aenig(1)	42·87	7·95	1·23	37·17	1·74	0·39	0·13	8·48	0·39	100·36	$XTi = 0·16$
	cpx(1)	50·31	1·31	0·86	27·93	0·77	0·47	7·76	10·17		99·59	$XFe_{tot} = 0·97$
9-6	gl(1)	71·21	0·21	10·96	5·96	0·47	0·02	0·22	6·01	4·95	89·68	
	amph(4)	47·73(63)	2·61(37)	0·74(14)	29·93(35)	1·64(20)	0·94(16)	1·82(36)	7·12(29)	1·38(11)	93·92	
	K-fsp(4)	67·42(120)	0·08(8)	15·91(109)	3·02(33)	0·04(8)	0·14(4)	0·01(3)	6·77(21)	6·50(62)	100·00	$Ab_{61}Or_{39}$
	aenig(2)	43·00(75)	8·31(17)	1·02(61)	38·28(30)	1·85(4)	0·32(15)	0·10(1)	8·04(18)	0·34(27)	101·26	$XTi = 0·16$
	cpx(2)	51·71(104)	1·86(15)	0·38(42)	27·47(93)	0·68(21)	0·34(5)	5·08(32)	11·79(1)		99·31	$XFe_{tot} = 0·98$
9-7	gl(1)	73·18	0·25	7·93	6·46	0·32	0·02	0·20	7·04	4·60	85·51	
	amph(4)	50·60(48)	1·92(20)	2·60(45)	26·14(104)	1·18(11)	0·59(6)	1·77(48)	7·75(66)	2·04(10)	94·58	
	K-fsp(3)	68·02(8)	0·05(5)	15·00(25)	3·26(35)	0·04(8)	0·13(5)	0·06(5)	6·80(44)	6·56(49)	100·00	$Ab_{61}Or_{39}$
	cpx(1)	50·35	2·01	0·74	25·81	0·77	0·40	5·60	13·93		99·59	$XFe_{tot} = 0·97$

(continued)

Table 3: Continued

Run-charge	Phase	SiO_2	TiO_2	Al_2O_3	FeO	MnO	MgO	CaO	Na_2O	K_2O	Total	Mole fractions
8-1	gl(8)	71·70(42)	0·45(4)	10·30(14)	7·29(22)	0·24(7)	0·09(2)	0·58(4)	4·63(74)	4·65(18)	91·20	
	Ti-mt(1)	1·04	15·36	0·34	80·28	1·53	0·27	−0·01	1·13	0·13	100·07	
8-2	gl(8)	72·50(22)	0·51(8)	10·60(16)	5·78(24)	0·26(11)	0·09(5)	0·46(4)	5·20(42)	4·54(15)	92·80	
	cpx(2)	51·20(8)	0·36(4)	0·42(35)	23·44(84)	1·57(15)	2·84(26)	17·86(110)	2·20(1)		99·89	$XFe_{tot} = 0·82$
8-3	gl(8)	71·50(34)	0·49(7)	10·20(12)	6·90(30)	0·28(7)	0·10(4)	0·46(6)	5·48(9)	4·60(13)	92·00	
	cpx(2)	50·24(5)	0·59(25)	0·35(27)	24·38(130)	2·01(69)	3·98(206)	16·35(258)	2·22(33)		100·12	$XFe_{tot} = 0·75$
8-4	gl(6)	71·18(45)	0·45(6)	10·31(9)	7·03(22)	0·26(13)	0·07(3)	0·45(10)	5·66(38)	4·59(11)	92·90	
	cpx(1)	50·90	0·37	0·94	24·42	1·45	2·26	16·37	2·89		99·60	$XFe_{tot} = 0·86$
8-5	gl(5)	71·10(25)	0·52(5)	9·37(7)	7·71(17)	0·38(8)	0·09(3)	0·50(19)	5·84(17)	4·51(18)	93·70	
	K-fsp(4)	66·38(26)	0·03(5)	17·66(30)	1·98(31)	0·03(5)	0·13(2)	0·11(4)	8·51(29)	5·10(26)	99·94	$Ab_{71}Or_{28}$
	cpx(1)	49·52	0·56	0·69	25·48	1·54	2·14	16·38	3·57		99·89	$XFe_{tot} = 0·87$
8-6	gl(6)	72·10(27)	0·63(5)	8·90(7)	7·36(23)	0·32(11)	0·08(3)	0·47(12)	5·69(19)	4·47(10)	94·50	
	K-fsp(4)	66·64(33)	0·01(4)	18·64(43)	1·03(25)	0·01(7)	0·17(8)	0·11(2)	8·02(21)	5·38(9)	99·96	$Ab_{69}Or_{30}$
	cpx(2)	50·82(64)	0·48(3)	1·05(19)	24·56(91)	1·39(6)	2·17(12)	15·60(89)	3·74(101)		99·81	$XFe_{tot} = 0·87$
8-7	gl(4)	71·10(24)	0·74(2)	6·94(25)	9·41(39)	0·31(6)	0·12(5)	0·65(9)	6·48(17)	4·28(16)	94·50	
	K-fsp(2)	66·31(56)	0·10(10)	18·32(3)	1·26(43)	0·02(5)	0·14(12)	0·15(28)	8·21(31)	5·39(4)	99·89	$Ab_{69}Or_{30}$
	cpx(1)	51·42	0·65	1·57	23·58	1·32	2·18	14·73	4·04		99·48	$XFe_{tot} = 0·87$
11-1	gl(4)	75·05(75)	0·37(9)	9·32(10)	6·13(60)	0·27(8)	0·05(4)	0·15(7)	4·83(89)	3·82(21)	87·67	
	K-fsp(2)	64·92(38)	0·00(0)	16·45(19)	2·24(17)	0·06(9)	0·12(11)	0·18(11)	6·87(3)	6·72(11)	97·56	$Ab_{60}Or_{39}$
	cpx(1)	49·45	1·08	0·40	26·78	1·19	9·88	1·61	9·70		100·09	$XFe_{tot} = 0·59$
	aenig(2)	39·41(62)	7·17(65)	1·10(1)	36·74(59)	1·45(31)	0·43(19)	0·36(7)	8·11(9)	0·19(0)	94·97	$XTi = 0·15$
11-2	gl(2)	76·17(42)	0·39(2)	7·48(2)	7·11(9)	0·39(2)	0·02(2)	0·12(4)	4·37(36)	3·94(32)	86·8745	
	K-fsp(1)	65·44	0·06	18·01	1·86	0·09	0·14	−0·02	7·35	6·95	99·89	$Ab_{62}Or_{38}$
	cpx(1)	53·13	2·54	0·14	25·77	0·66	0·16	1·98	14·36		98·74	$XFe_{tot} = 0·99$
	amph(1)	52·94	2·25	1·08	29·89	1·21	0·60	0·78	9·35	1·68	99·78	
	aenig(1)	42·89	8·49	0·50	37·81	1·61	0·33	0·17	8·07	0·17	100·03	$XTi = 0·17$
11-3	gl(1)	70·74	0·29	11·17	5·51	0·34	0·05	0·06	6·52	5·33	93·42	
	K-fsp(1)	64·26	0·05	14·44	4·02	0·16	0·13	0·05	7·14	6·08	96·32	$Ab_{64}Or_{36}$
	cpx	n.d.										
	amph(1)	46·49	2·01	0·94	28·32	1·38	0·93	1·56	8·41	1·33	91·38	
5-1	gl(7)	70·30(27)	0·48(4)	10·00(11)	7·48(19)	0·28(12)	0·05(4)	0·54(4)	6·27(29)	4·60(7)	96·00	
	cpx(3)	49·97(54)	0·67(5)	1·14(31)	24·17(53)	1·54(10)	2·02(15)	16·30(93)	4·10(71)		99·91	$XFe_{tot} = 0·88$
5-2	gl(2)	70·10(55)	0·46(4)	9·95(13)	7·41(36)	0·51(23)	0·06(3)	0·49(7)	6·38(15)	4·61(8)	96·90	
	cpx(3)	49·66(160)	0·55(9)	0·99(115)	23·47(152)	1·43(6)	2·59(29)	16·87(149)	4·19(40)		99·75	$XFe_{tot} = 0·84$
5-3	gl(9)	69·90(60)	0·50(6)	9·56(20)	8·03(39)	0·30(25)	0·09(4)	0·69(45)	6·42(21)	4·52(12)	97·10	
	K-fsp(3)	66·30(36)	0·04(1)	18·65(24)	1·09(19)	0·06(8)	0·10(1)	0·08(9)	8·52(17)	5·23(5)	100·06	$Ab_{71}Or_{29}$
	cpx(3)	49·80(163)	0·78(44)	1·26(73)	24·14(190)	1·31(6)	2·37(22)	15·83(140)	4·23(74)		99·73	$XFe_{tot} = 0·86$
5-4	gl(9)	71·10(249	0·53(6)	8·98(17)	8·09(50)	0·34(18)	0·08(3)	0·50(6)	5·90(28)	4·43(11)	97·00	
	K-fsp(3)	66·52(39)	0·14(11)	17·60(100)	1·88(78)	0·08(8)	0·16(7)	0·21(27)	8·37(15)	4·98(17)	99·94	$Ab_{71}Or_{28}$
	cpx(3)	50·02(153)	0·41(5)	1·68(106)	24·09(182)	1·30(12)	1·97(5)	16·49(126)	3·89(65)		99·80	$XFe_{tot} = 0·88$
5-5	gl(6)	71·30(25)	0·53(7)	8·37(12)	8·55(54)	0·42(20)	0·08(1)	0·55(12)	5·82(30)	4·43(7)	97·30	
	K-fsp(5)	66·40(49)	0·06(10)	17·63(74)	1·94(62)	0·08(7)	0·12(4)	0·06(2)	8·40(16)	5·07(10)	99·77	$Ab_{71}Or_{28}$
	cpx(1)	48·94	0·49	0·32	25·96	1·36	2·00	17·22	3·62		99·91	$XFe_{tot} = 0·88$
5-6	gl(5)	71·20(63)	0·58(7)	8·40(27)	8·70(44)	0·40(10)	0·11(1)	0·58(6)	5·63(34)	4·41(6)	97·80	
	K-fsp(4)	66·57(19)	0·13(6)	17·12(83)	2·33(43)	0·01(15)	0·12(5)	0·12(8)	8·45(24)	4·96(17)	99·80	$Ab_{72}Or_{28}$
	cpx(1)	50·42	0·55	0·89	25·96	1·54	1·64	15·14	4·37		100·51	$XFe_{tot} = 0·90$

(continued)

Table 3: Continued

Run-charge	Phase	SiO_2	TiO_2	Al_2O_3	FeO	MnO	MgO	CaO	Na_2O	K_2O	Total	Mole fractions
5-7	gl(4)	66·00(34)	1·06(8)	5·39(64)	14·20(57)	0·72(14)	0·14(5)	0·96(16)	7·38(6)	4·20(18)	98·10	
	K-fsp(4)	66·55(36)	0·09(6)	18·07(37)	1·27(22)	0·05(7)	0·12(6)	0·03(5)	8·12(31)	5·65(23)	99·96	$Ab_{68}Or_{31}$
	Fe°(1)	0·58	0·00	0·10	97·88	0·01	0·09	0·04	1·23	0·13	99·96	
6-1	gl(10)	71·90(45)	0·43(6)	9·70(93)	7·03(82)	0·26(10)	0·07(3)	0·31(10)	5·73(37)	4·55(28)	93·60	
	K-fsp(4)	65·55(36)	0·09(14)	17·88(8)	2·22(28)	0·11(2)	0·11(9)	0·18(8)	7·90(7)	5·90(8)	99·95	$Ab_{67}Or_{33}$
	cpx(1)	51·14	0·49	1·54	25·92	1·55	1·40	13·81	3·87		99·72	$XFe_{tot} = 0·92$
6-2	gl (10)	72·40(30)	0·54(10)	8·35(47)	8·00(37)	0·34(13)	0·07(2)	0·29(10)	5·66(26)	4·39(13)	93·40	
	K-fsp(4)	66·24(59)	0·07(12)	17·50(54)	2·48(24)	0·02(4)	0·14(3)	0·14(5)	7·83(18)	5·51(8)	99·92	$Ab_{68}Or_{31}$
	cpx(1)	49·77	1·08	0·95	26·11	1·20	1·97	12·84	6·17		100·09	$XFe_{tot} = 0·89$
6-3	gl(10)	72·60(41)	0·61(6)	7·62(22)	8·65(36)	0·36(12)	0·08(2)	0·30(6)	5·46(37)	4·32(10)	94·20	
	K-fsp(2)	66·18(29)	0·10(6)	18·18(13)	1·59(2)	0·06(3)	0·19(7)	0·06(2)	7·95(1)	5·67(22)	99·98	$Ab_{68}Or_{32}$
	cpx(2)	50·41(42)	0·44(25)	0·29(6)	17·34(14)	1·00(9)	1·01(14)	8·54(85)	3·63(101)		82·67	$XFe_{tot} = 0·91$
	Ilm	n.d.										
6-4	gl(10)	72·40(28)	0·70(5)	7·03(10)	9·10(32)	0·42(16)	0·09(2)	0·34(8)	5·66(35)	4·25(5)	93·80	
	K-fsp(6)	66·26(13)	0·07(9)	16·45(89)	3·49(79)	0·01(8)	0·07(4)	0·10(14)	7·82(15)	5·68(10)	99·93	$Ab_{67}Or_{32}$
	cpx(3)	48·97(58)	0·90(11)	0·38(28)	27·27(56)	1·47(6)	1·65(14)	14·36(107)	4·70(49)		99·70	$XFe_{tot} = 0·91$
6-5	gl(10)	72·10(40)	0·61(11)	6·69(26)	9·64(43)	0·39(9)	0·09(4)	0·33(4)	5·89(48)	4·30(17)	94·50	
	K-fsp(3)	66·26(11)	0·02(4)	17·93(17)	1·83(23)	0·01(10)	0·15(11)	0·01(2)	7·93(28)	5·79(5)	99·86	$Ab_{68}Or_{32}$
	cpx(2)	48·44(15)	0·85(16)	0·61(4)	27·75(1)	1·98(26)	2·93(3)	13·31(12)	4·01(20)		99·90	$XFe_{tot} = 0·85$
6-6	gl(10)	71·70(49)	0·70(5)	6·59(16)	10·10(33)	0·40(11)	0·09(5)	0·37(6)	5·78(72)	4·29(15)	94·40	
	K-fsp(2)	66·41(17)	0·10(7)	17·55(1)	2·01(6)	0·01(2)	0·17(1)	0·11(10)	7·67(11)	5·69(15)	99·71	$Ab_{67}Or_{33}$
	cpx(2)	46·07(19)	2·22(28)	0·40(10)	29·57(104)	1·45(6)	2·83(2)	11·30(28)	6·07(13)		99·90	$XFe_{tot} = 0·87$
6-7	gl(10)	69·00(41)	0·47(9)	4·72(19)	12·80(49)	0·63(16)	0·13(3)	0·77(7)	7·34(79)	4·17(16)	94·40	
	K-fsp(3)	66·7(39)	0·09(17)	17·2(54)	2·09(85)	0·04(4)	0·14(4)	0·01(6)	7·36(10)	6·28(5)	99·87	$Ab_{64}Or_{36}$
	cpx	n.d.										
	aenig(1)	47·35	6·85	1·30	32·98	1·00	0·68	0·37	8·29	1·09	94·14	
10-1	gl	n.d.										
	K-fsp(2)	65·60(23)	0·09(7)	16·33(60)	3·43(62)	0·03(16)	0·19(0)	0·16(5)	7·11(30)	6·96(75)	100·00	$Ab_{60}Or_{39}$
	amph(1)	48·78	0·50	5·16	14·10	0·44	0·37	2·23	8·02	1·94	81·54	
	cpx(2)	56·29(64)	1·12(1)	3·11(17)	21·61(42)	0·85(15)	0·56(6)	4·63(19)	10·46(30)		98·62	$XFe_{tot} = 0·96$
	Ti-mt	n.d.										
10-2	gl	n.d.										
	K-fsp(2)	67·14(4)	0·03(8)	14·85(8)	3·98(41)	0·09(7)	0·06(11)	0·10(15)	6·94(6)	6·49(2)	100·00	$Ab_{62}Or_{38}$
	amph(1)	54·26	1·62	3·97	18·86	1·30	0·81	0·95	8·12	2·55	92·44	
	cpx(2)	53·58(14)	2·00(32)	1·41(9)	25·31(5)	0·74(19)	0·39(2)	3·45(91)	12·42(95)		99·31	$XFe_{tot} = 0·97$
10-3	gl	n.d.										
	K-fsp(1)	66·32	0·02	15·49	3·89	0·05	0·13	0·10	6·91	6·73	100·00	$Ab_{61}Or_{39}$
	amph(2)	52·36(54)	3·48(9)	1·77(20)	26·56(15)	1·47(10)	1·2′(22)	1·26(45)	10·0(31)	1·60(11)	100·00	
10-4	gl	n.d.										
	K-fsp(4)	67·71(51)	0·01(13)	14·91(83)	3·78(76)	0·02(3)	0·10(9)	0·07(4)	7·28(10)	5·98(8)	100·00	$Ab_{65}Or_{35}$
	amph(2)	51·61(54)	3·10(59)	0·82(19)	29·33(88)	1·68(68)	0·93(56)	0·60(2)	10·4(67)	1·42(8)	100·00	
	cpx(2)	54·52(51)	2·46(8)	1·65(35)	23·99(82)	0·59(8)	0·41(11)	3·64(67)	11·93(50)		99·20	$XFe_{tot} = 0·97$
7-1	gl(9)	71·70(32)	0·54(8)	8·93(10)	7·79(29)	0·26(9)	0·07(3)	0·41(6)	5·82(8)	4·49(10)	93·90	
	K-fsp(4)	66·45(50)	0·06(11)	18·20(13)	1·70(11)	0·02(1)	0·15(2)	0·05(6)	8·16(9)	5·18(3)	99·99	$Ab_{70}Or_{29}$
	cpx(4)	48·01(208)	0·58(28)	0·79(76)	24·31(92)	1·66(30)	2·58(94)	16·21(175)	3·98(79)		98·12	$XFe_{tot} = 0·85$
7-2	gl(8)	72·00(32)	0·51(8)	8·83(76)	7·49(59)	0·29(15)	0·07(3)	0·42(10)	5·86(34)	4·57(12)	95·00	
	K-fsp(3)	66·51(32)	0·11(12)	18·14(20)	1·70(14)	0·03(11)	0·13(6)	0·01(7)	8·06(12)	5·26(13)	99·92	$Ab_{70}Or_{30}$
	cpx(4)	49·76(162)	0·48(10)	1·03(114)	24·95(150)	1·57(23)	2·26(16)	16·02(198)	3·86(102)		99·94	$XFe_{tot} = 0·87$

(continued)

Table 3: Continued

Run-charge	Phase	SiO_2	TiO_2	Al_2O_3	FeO	MnO	MgO	CaO	Na_2O	K_2O	Total	Mole fractions
7-3	gl(10)	72·80(46)	0·61(5)	7·9(14)	8·00(34)	0·40(15)	0·08(3)	0·45(7)	5·35(65)	4·40(13)	94·20	
	K-fsp(3)	66·66(19)	0·07(7)	17·66(23)	2·03(8)	0·04(6)	0·06(11)	0·08(7)	8·05(11)	5·29(11)	99·94	$Ab_{70}Or_{30}$
	cpx	n.d.										
7-4	gl(8)	73·20(78)	0·60(9)	7·79(22)	8·08(31)	0·36(8)	0·09(4)	0·44(8)	4·96(43)	4·45(9)	94·00	
	K-fsp(4)	66·70(41)	0·03(10)	17·72(55)	1·89(27)	0·10(10)	0·17(6)	0·03(5)	8·16(10)	5·08(14)	99·89	$Ab_{71}Or_{29}$
	cpx(1)	50·14	0·56	0·20	25·51	1·57	1·98	16·78	3·16		99·90	$XFe_{tot} = 0·88$
7-5	gl(10)	71·60(40)	0·81(8)	6·69(24)	9·33(37)	0·42(11)	0·13(3)	0·58(9)	6·04(17)	4·42(12)	95·00	
	K-fsp(5)	67·69(72)	0·21(21)	16·20(109)	2·81(85)	0·07(9)	0·07(9)	0·20(16)	7·47(36)	5·11(23)	99·84	$Ab_{68}Or_{31}$
	cpx(2)	49·39(47)	0·49(3)	0·49(1)	28·83(31)	1·79(7)	1·77(8)	14·61(12)	2·58(7)		99·95	$XFe_{tot} = 0·90$
7-6	gl(7)	72·28(31)	0·69(6)	7·23(15)	8·40(41)	0·40(8)	0·10(2)	0·47(7)	6·02(17)	4·40(7)	95·60	
	K-fsp(4)	65·92(59)	0·08(9)	16·84(66)	2·63(29)	0·04(7)	0·14(8)	0·05(6)	8·14(24)	5·04(33)	98·88	$Ab_{71}Or_{28}$
	cpx(1)	48·37	0·38	2·11	24·80	1·36	2·11	16·05	4·46		99·64	$XFe_{tot} = 0·88$
7-7	gl(7)	71·97(48)	0·71(3)	6·60(24)	9·23(29)	0·39(159	0·11(3)	0·62(6)	5·97(38)	4·41(11)	94·20	
	K-fsp(4)	67·18(47)	0·01(17)	17·65(28)	1·73(21)	0·01(13)	0·07(7)	0·05(2)	7·93(26)	5·34(4)	99·94	$Ab_{69}Or_{31}$
	cpx(1)	47·97	0·58	2·21	26·04	1·68	1·66	16·16	3·73		100·03	$XFe_{tot} = 0·91$

[1]Glass analyses normalized to 100% anhydrous, with all Fe as FeO. Unnormalized total is reported.
[2]Number of microprobe analyses performed.
[3]One standard deviation in terms of last digit.
Ti-magnetite composition of charge 3-16 was used for mass-balance calculation in charges where Ti-magnetite was too small to be probed (charges 2-8, 2-9, 2-10, 2-11, 2-12, 3-19, 4-1 and 4-2). XFe_{tot} is molar Fe/(Fe + Mg) with all Fe as Fe^{2+}. *X*Ti is molar Ti/(Ti + Fe) with all Fe as Fe^{2+}. gl, glass; K-fsp, K-feldspar; cpx, clinopyroxene; aenig, aenigmatite; amph, amphibole; Ti-mt, Ti-magnetite; n.d., not determined.

showed glass contamination, revealed by K_2O concentrations >0·1 wt %. In charges where glass composition could be determined, the glass contribution to clinopyroxene analyses was calculated by first assuming a zero content of K_2O in clinopyroxene to evaluate the glass proportion (thus equal to $K_2O_{analysis}/K_2O_{glass}$), and then using that proportion (found to be in most cases below 15%, but up to 40% for a few analyses) to recalculate the actual clinopyroxene compositions. Restored clinopyroxene analyses have oxide totals between 99 and 100 wt %, with Al_2O_3 lower than 1 wt % and SiO_2 contents comparable with their natural counterparts. Ti-magnetite and ilmenite are always smaller than 3 μm, which makes it impossible to obtain reliable EMP analyses. Glass was analysed in all charges, except for those near solidus at 680°C, where the glass pools were too small to be probed. The presence of large bubbles (30–50 μm in diameter) in almost all charges is taken as evidence of fluid saturation.

Phase proportions

The amount of residual liquid varied from 100 wt % to less than 10 wt % in charges close to the solidus. The most abundant phase is alkali feldspar, with mass proportions varying from trace amounts to over 60 wt % in near-solidus charges (charge 9-7, Table 2). Such a proportion of feldspar is similar to that obtained in near fully crystallized comendite magmas by Scaillet & Macdonald (2003). Despite the significant scatter displayed by the dataset (in large part related to the difficulty in determining accurately dissolved melt water contents below 2–3 wt %), at any given temperature, the amount of feldspar tends to increase with decreasing H_2O_{melt} (Fig. 2), the slope of each trend increasing with temperature. Quartz is generally next in abundance when present, and reaches 15 wt % in the most crystallized charges whose glasses could be analysed (charge 9-7). This is significantly lower than in equivalent charges obtained from comendite near-complete crystallization by Scaillet & Macdonald (2003), in which the quartz mass proportion goes up to 30 wt %. The reason for such a difference is possibly the greater amount of iron in pantellerite relative to comendite (twice as much), which allows a greater proportion of silicate ferro-magnesian phases to crystallize near the solidus (amphibole at 150 MPa), and also the lower silica content of our starting material. It is worth stressing that both the feldspar and quartz modal proportions in our experiments are similar to those of felsic enclaves hosted by pantellerites (Ferla & Meli, 2006). The amount of clinopyroxene in the experiments never exceeds 10 wt %, and is usually below 6 wt % (Fig. 3a), whereas that of amphibole can reach 21 wt % in some crystal-rich charges. Aenigmatite proportion is below 9 wt %, but usually is in the range 1–3 wt

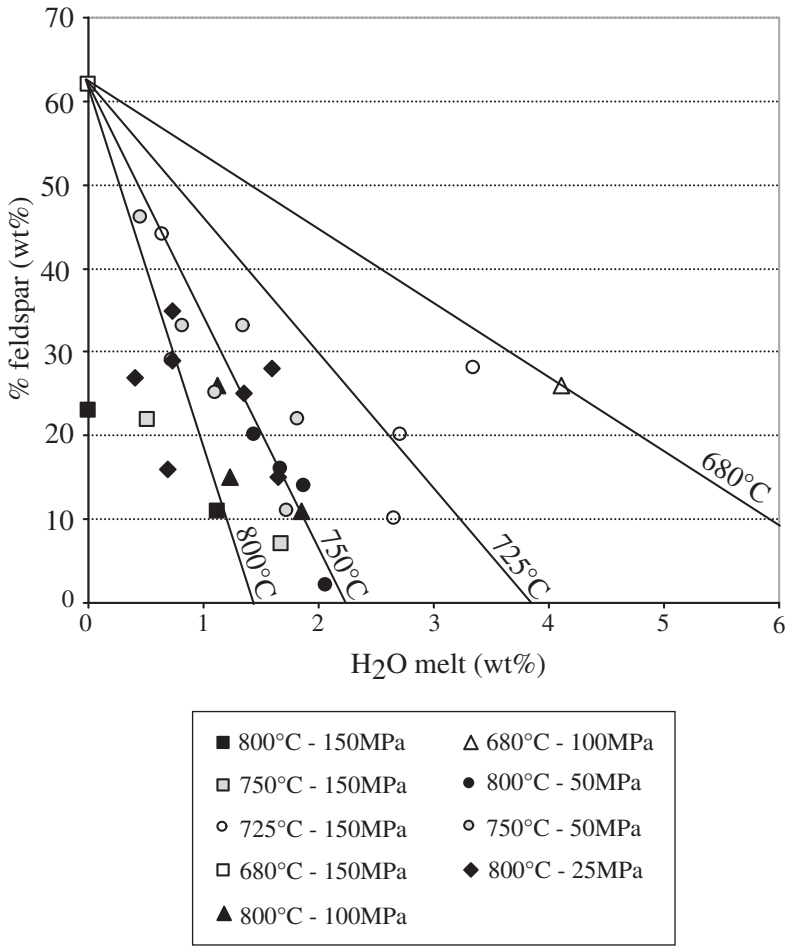

Fig. 2. Variation of feldspar weight per cent in experimental charges vs melt water content (H_2O_{melt}). Lines are hand-drawn best estimates of the isothermal variation of feldspar proportion with melt water content. They converge towards a single point, which is taken to be the feldspar abundance under dry conditions. This is equivalent to assuming that there is no pressure effect on the dry solidus, a reasonable assumption for the pressure range investigated.

%, whereas the amount of Fe–Ti oxides is no more than 2 wt %. The mass ratio of feldspar to clinopyroxene ranges between unity and up to 20 for charges in which the phase proportions are reasonably well known, with no obvious correlation with either H_2O_{melt} or temperature of synthesis (Fig. 3b). However, charges obtained at 50 MPa, and some of those at 25 MPa, tend to lie at the higher end of the range, which suggests that the crystallization of pantellerite magma at very low pressure favours feldspar over pyroxene. Apart from this low-pressure group, the vast majority of charges has a feld/cpx ratio of around 3–7, which brackets that of the starting rock (5·8).

Phase equilibria

The phase relationships at 150 MPa are shown in Fig. 4a. At H_2O saturation (*c.* 6 wt % H_2O_{melt}) clinopyroxene is the liquidus phase, appearing at 760°C, followed by alkali feldspar and then by quartz whose crystallization is inferred to occur at around 650°C. This relative order of crystallization of the silicate phases persists over the enire range of investigated T–H_2O_{melt}. Magnetite replaces clinopyroxene as the liquidus phase at H_2O_{melt} lower than 4 wt %. Aenigmatite is stable at temperatures below 740°C under H_2O_{melt} poor conditions, and below 680°C at $H_2O \leq 5$ wt %. Amphibole begins to crystallize at temperatures lower than 700°C, and its stability field is drawn as nearly independent of melt water content, by analogy with the better constrained stability fields of amphibole in compositionally similar Kenyan rhyolites (Scaillet & Macdonald, 2001, 2006). Ilmenite was detected in only one charge, at 750°C and 1·7 wt % H_2O_{melt}.

Although less tightly constrained than at 150 MPa, phase relationships at 100 MPa (Fig. 4b) show broadly the same pattern as at 150 MPa, with clinopyroxene being the liquidus phase, followed by alkali feldspar and then quartz. Amphibole begins to crystallize at $T < 700$°C, but is not

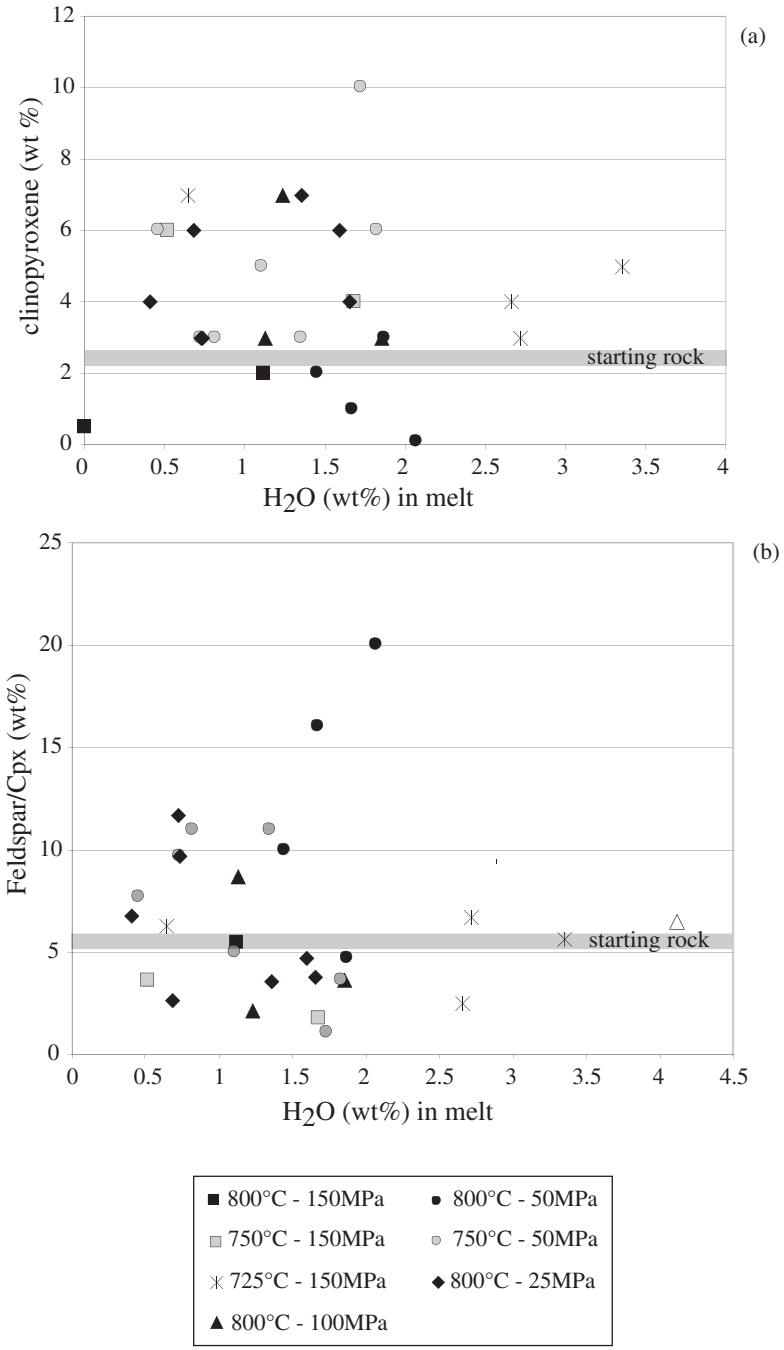

Fig. 3. (a) Variation of clinopyroxene proportions (wt %) in experimental charges with melt water content (H_2O_{melt}); (b) variation of Feldp/Cpx weight ratio in experimental charges. In both panels the grey bands correspond to the parameter value in the starting rock.

stable at H_2O saturation at 680°C, therefore having a negatively sloping stability curve under H_2O-rich conditions. Aenigmatite displays the opposite behaviour, its stability field being limited to water contents >2·5 wt % at around 680°C.

The isobaric section at 50 MPa (2·7 wt % H_2O_{melt} at saturation) is similar to that at 100 MPa (Fig. 4c), except that aenigmatite could be identified only in one charge near the solidus, hence this phase is shown with a very restricted stability field at this pressure. Clinopyroxene is the liquidus phase and alkali feldspar appears before quartz, both phases crystallizing closer to each other than they do at higher pressures (note that the quartz boundary in Fig. 4c does not strictly fit with the phase

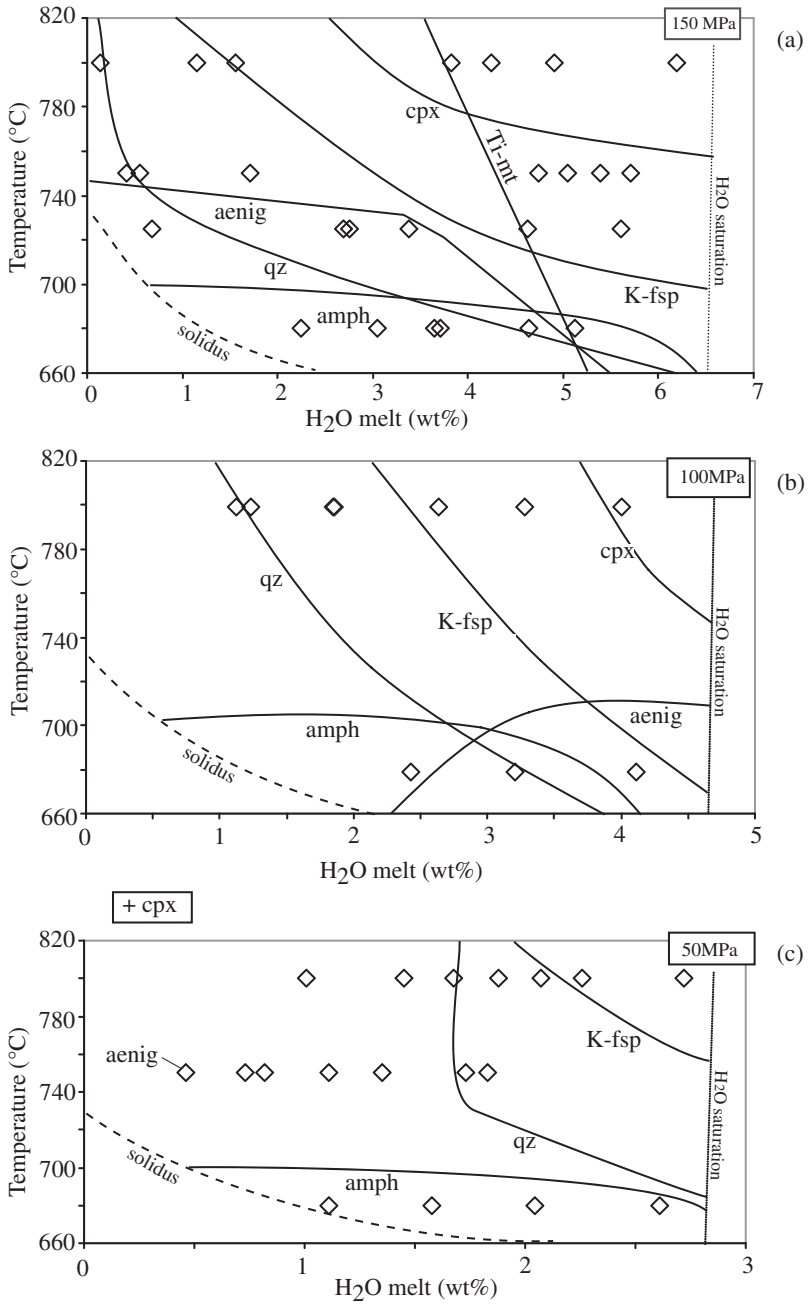

Fig. 4. Isobaric–polythermal phase relationships of PAN 01113 pantellerite at: (a) 150 MPa, (b) 100 MPa and (c) 50 MPa. cpx, clinopyroxene; K-fsp, alkali feldspar; qz, quartz; amph, amphibole; aenig, aenigmatite. H_2O melt, H_2O dissolved in the melt (see text). In the three panels the approximate location of the solidus is indicated by dashed lines, whereas the inferred curve for water saturation is shown as dotted near-vertical lines. It should be noted that, for simplicity, we assume that the temperature effect on water solubility is negligible, although our data suggest that this might not strictly be the case. However, the by-difference method does not allow us to obtain sufficiently accurate results to evaluate any temperature dependence of water solubility in our melt compositions.

assemblages in run products given in Table 2, owing to the large errors associated with the determination of the H_2O content of the melt using the by-difference method over a narrow range of water contents, as at 50 MPa). Amphibole crystallization occurred again only in the 680°C run and is inferred to have a broadly flat in-curve shape similar to that suggested for higher pressures.

Under the explored conditions, aenigmatite was never found in coexistence with either Ti-magnetite or ilmenite,

suggesting that these phases may be in peritectic relationship with each other (Nicholls & Carmichael, 1969).

The isothermal phase equilibria in P–H_2O_{melt} space are shown in Fig. 5 at three temperatures (800°C, 750°C and 680°C). Such polybaric sections allow us to explore the effect of decompression on pantellerite phase equilibria. The sections at 800°C and 750°C are almost identical (Fig. 5a and b), with clinopyroxene, alkali feldspar and quartz saturation curves all having negative slopes. Near-isothermal ascent at fixed H_2O_{melt} of a pantellerite melt would thus promote crystallization. At 750°C, the clinopyroxene and alkali feldspar primary fields are enlarged toward higher H_2O_{melt} as compared with the 800°C section. At both temperatures, quartz crystallization is restricted to low water contents (<2 wt %). Phase relationships at 680°C (Fig. 5c) show significant differences with respect to the higher-T sections: clinopyroxene and alkali feldspar are the liquidus phases, whereas quartz is stable over a wider range of H_2O_{melt} (<4·6 wt %), having a steeper in-curve than at higher temperatures. Amphibole is present in all the charges, except at H_2O saturation at 100 MPa. The projections highlight that aenigmatite is stable near the liquidus essentially at $P>100$ MPa and requires water-rich conditions to crystallize in crystal-poor pantellerites.

Phase compositions

Except for alkali feldspar, the compositions of the glass, clinopyroxene, aenigmatite, amphibole and Ti-magnetite (whenever possible), were determined by EMP. Feldspar analyses were mostly obtained by SEM–EDS, because of the difficulties in distinguishing it from the surrounding glass with our current EMP imaging system. In charges where feldspar could be analysed by both EMP and SEM–EDS, essentially identical compositions were retrieved. Feldspar analyses were considered acceptable when their structural formulae fulfilled the criteria: $[Ca+Na+K]=1{\cdot}000\pm0{\cdot}030$ and $[Si+Al+Fe]=4{\cdot}000\pm0{\cdot}010$ a.p.f.u. (calculated on a 8 oxygen basis).

The composition of experimental feldspars falls in the range $Or_{28–53}$, thus reproducing natural phenocryst compositions in pantellerites, and is also within the compositional range of feldspars synthesized from Kenyan peralkaline rhyolite starting materials (Scaillet & Macdonald, 2003, 2006). Compositional trends displayed by feldspar are essentially governed by variations in H_2O_{melt} and, to a lesser extent, by temperature and pressure. A broad positive correlation is apparent between Or and H_2O_{melt} when all the data are plotted together (Fig. 6). However, when considering the subset of data for each temperature, the group at 800°C defines a negative correlation with H_2O_{melt}, most compositions falling in the range Or_{28}–Or_{33}. At 750–725°C a nearly vertical trend in the range Or_{30}–Or_{35} is obtained whereas the 680°C group defines a clear positive trend with H_2O_{melt}, the Or content ranging from Or_{35} to Or_{53} at 150 MPa (Fig. 6). As stressed above for feldspar proportions (Fig. 2), the difficulties in determining accurately dissolved water contents below 2 wt % probably explain the lack of clear correlation for the feldspars in this H_2O domain. Although the CaO content is always very low (<0·26 wt %), making it difficult to determine with SEM–EDS, it increases generally with H_2O_{melt} at any given temperature. Similarly, CaO seems to increase with pressure and temperature, being barely detectable at 25 MPa (Table 3).

Pyroxene composition varies significantly with the experimental parameters. Calculation of the amount of Fe^{3+} from restored pyroxene analyses using the method of Lindsley (1983) yields Fe^{3+} between 20% at 800°C and 70–100% (i.e. aegirine) at 680°C. Besides this variation, however, there is no obvious correlation of $X\mathrm{Fe}^{2+}$ [$=\mathrm{Fe}^{2+}/(\mathrm{Fe}^{2+}+\mathrm{Mg})$, atomic] with the experimental parameters. This is probably related in part to inaccuracies in Fe^{3+} estimates based on stochiometric considerations, but also to the fact that the amount of Fe^{3+} is controlled by structural effects in addition to intensive parameters (e.g. fO_2). In contrast, the $X\mathrm{Fe}_{tot}$ ratio [$\mathrm{Fe}_{tot}/(\mathrm{Fe}_{tot}+\mathrm{Mg})$, atomic] displays good correlations with both temperature and fO_2. It varies between 0·84–0·9 at 800°C and 0·92–0·99 at 680°C (Fig. 7). It should be noted that changes in fH_2O (i.e. H_2O_{melt}) along any given isotherm produce variations in fO_2, which in turn affect $X\mathrm{Fe}_{tot}$ (Fig. 7). The covariation of $X\mathrm{Fe}_{tot}$ with both temperature and fO_2 has been parameterized with the following empirical expression:

$$T = 1568 - 25\cdot64\ \Delta\mathrm{NNO} - 958\ \mathrm{XFe}_{tot} \times (R^2 = 0\cdot86, \mathrm{SE} = 13\cdot4)$$

where ΔNNO is the fO_2 expressed relative to the NNO buffer, and T is the temperature in °C. This expression has been derived using charges with H_2O_{melt} higher than 1 wt %, because below this H_2O_{melt} threshold the errors in fO_2 estimates of the experimental charges can be large (see above). The expression back-calculates experimental temperatures within ±13°C. The average clinopyroxene–liquid exchange coefficient ($K\mathrm{d}^{\mathrm{Fe–Mg}}{}_{\mathrm{cpx\text{-}liq}}$, calculated with $\mathrm{FeO}=\mathrm{FeO}_t$) is $0{\cdot}16\pm0{\cdot}14$ (the large standard deviation is due to the low to very low MgO content of the experimental pyroxenes), which is similar to the value found by Scaillet & Macdonald (2003) and to that between the Ca-rich pyroxene and groundmass of the starting rock (0·14, Table 1).

The Na and Ca contents of the experimental pyroxenes show a large variation from augite to aegirine–augite to aegirine (charges 11-1 and 9-4), with Na_2O contents varying from 2·3 wt % (charge 8-3) to 14·4% at 680°C (charge 11-2), thus reproducing the compositional range displayed by phenocrysts and microlites in the starting rock (Table 1). Changes in either Na or Ca are driven by

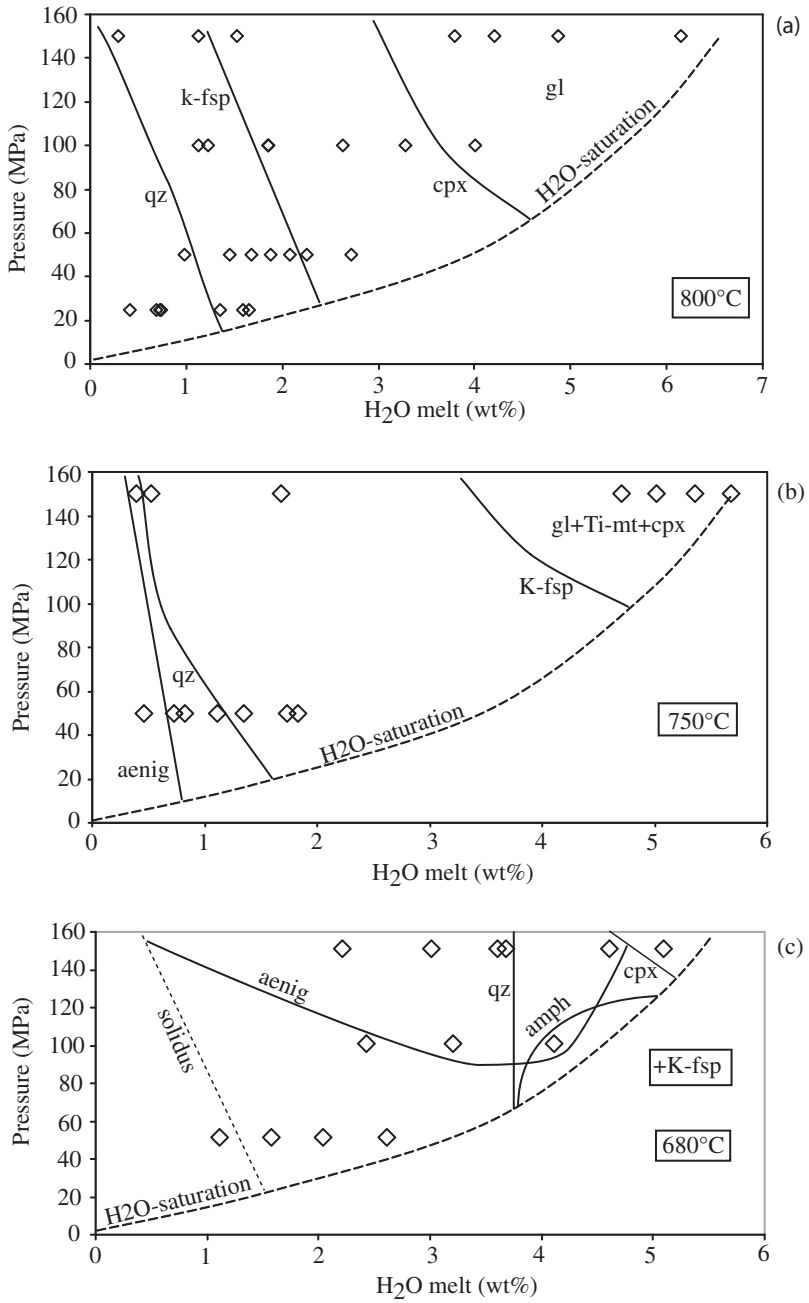

Fig. 5. Isothermal–polybaric phase relationships of PAN 01113 pantellerite at: (a) 800°C, (b) 750°C and (c) 680°C. In (c) alkali feldspar and clinopyroxene are always present. The dashed lines represent the water saturation curve experimentally derived for the PAN 01113 composition (Di Carlo *et al.*, in preparation).

variations in H_2O_{melt} and temperature (Fig. 8). As a rule, although some scatter is apparent, the CaO content of clinopyroxene appears to increase with temperature and, to a lesser extent, with melt water content (Fig. 8). Although at any fixed temperature, pyroxene Ca–Na contents change continuously, in detail two groups of pyroxenes can be distinguished (Fig. 9): (1) the first group is characterized by low Na and high Ca contents and typifies pyroxene from high-temperature runs (800–725°C); (2) the second group has high-Na and low-Ca and characterizes pyroxene crystallized at 680°C. It is unclear whether this represents a lack of data in the temperature

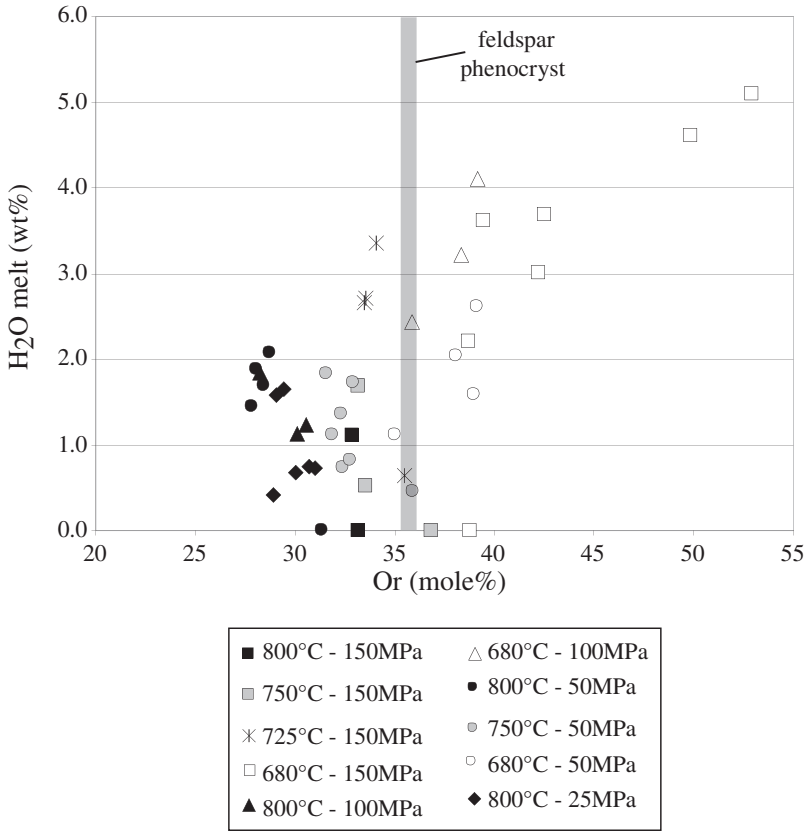

Fig. 6. Variation of the Or content (mol %) of experimental alkali feldspars with melt water content (H_2O_{melt}) at a range of temperatures and pressures. The grey band corresponds to the average Or content of alkali feldspar phenocryts in the starting rock.

range 725–680°C or if such a compositional gap reflects the presence of a solvus along the aegirine–augite join. TiO_2 also varies, primarily with temperature, from around 0·4 wt % at 800°C to 2·4 wt % at 680°C.

Amphibole composition spans the range arfvedsonite–Fe-eckermannite (Leake, 1997). Amphibole is FeO and Na_2O rich (31·3 and 10·4 wt %, as maximum contents, respectively) and MnO–MgO poor (up to 1·3 and 1·5 wt %, respectively), closely reproducing the phenocryst composition, notably under H_2O-rich conditions. Its *X*Fe ratio is mostly in the range 0·91–0·95 and thus approaches that of the natural microlites (0·97, Table 1) and shows no apparent variation with either pressure or H_2O_{melt}. Coexisting amphibole and sodic clinopyroxene have nearly the same *X*Fe (Table 3). Although amphibole crystallizes only in low-temperature runs, the trend of increasing Na in amphibole with increasing peralkalinity index (PI) of the glass is clear. Such a trend reflects the increase in the Na_2O content of the residual liquid with crystallization. This behaviour is also mirrored by variations in the calcium content of amphibole, which appears to compensate that of sodium; potassium remains broadly constant over the pressure range investigated here (between 1 and 2 wt % K_2O, although the 150 MPa amphiboles have K_2O contents close to 1 wt %; Table 3). As a result the Ca content of amphibole strongly increases with H_2O_{melt}, regardless of the pressure of synthesis (Fig. 10). Such a positive correlation has been previously noted by Scaillet & Macdonald (2003) in their experiments on Kenyan peralkaline rhyolites, and confirms that the Ca content of sodic amphibole is a good hygrobarometer for peralkaline felsic magmas. We stress however, that the trends are bulk-rock composition specific (Fig. 10).

Aenigmatite is fairly constant in composition, as in natural rocks (Nicholls & Carmichael, 1969): It has a $[Ti/(Fe+Ti)] \times 100 = 16{\cdot}6 \pm 0{\cdot}6$, with some lower values (13·6–14·9) being found as outliers in low-temperature runs (charges 9-2, 9-4 and 11-1).

The variation of glass composition with degree of crystallization is shown in Figs 11 and 12, and resembles that established in previous experiments performed on similar rocks (Scaillet & Macdonald, 2003, 2006). The major features of the melt compositional variations

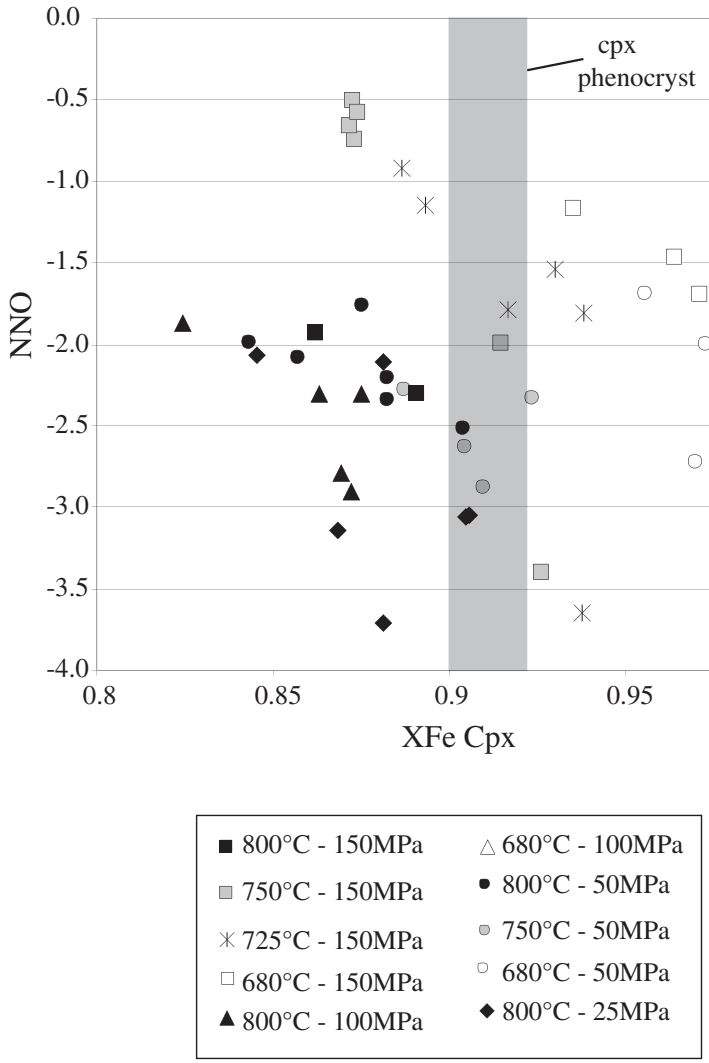

Fig. 7. Variation of $X\mathrm{Fe}_{tot}$ [$\mathrm{Fe}_{tot}/(\mathrm{Fe}_{tot}+\mathrm{Mg})$] of experimental clinopyroxenes with oxygen fugacity expressed as ΔNNO at a range of temperatures and pressures. The grey band corresponds to the average *X*Fe value of clinopyroxene phenocrysts in the starting rock.

are (1) a pronounced increase in FeO_{tot} and Na_2O, and (2) a decrease in SiO_2, Al_2O_3 and K_2O contents (to 66, 4·7 and 3·9 wt % respectively) as crystallization proceeds. The melt peralkalinity index varies from 1·2 to a maximum of 3·5, with the majority of glasses being within the interval 1·5–2·0. The most iron-rich liquid produced in our experiments has nearly 15 wt % FeO, for a silica content of about 65 wt %, which is well beyond the maximum iron content reported so far for erupted rhyolites at Pantelleria (8·8 wt %) or elsewhere (Fig. 11). The silica content of the residual liquids first increases until a melt fraction of 0·5 is reached, and thereafter decreases as a result of the greater abundance of quartz in the crystallizing assemblage (Fig. 12a). A similar behaviour is noted for TiO_2, which steadily increases until aenigmatite starts to crystallize (Fig. 12b). Cl increases steadily with increasing magma crystallization, reaching concentrations in excess of 1 wt % in the most crystallized charges (Fig. 12d). In detail two sub-trends appears for Cl in Fig. 12, whose origin is still unclear, but could be related to slight differences in fO_2 and associated changes in Fe^2/Fe^3 of the melt (Di Carlo *et al.*, in preparation).

When whole-rock compositions (felsic) from Pantelleria are plotted together with our experimental data, there is a significant overlap between experimental and natural trends, which suggests that the experimental conditions explored here faithfully reproduce those prevailing in the magma reservoir (Fig. 11). Of interest in the context of this study are the residual melts produced when clinopyroxene is the sole crystallizing phase. Under such conditions, the

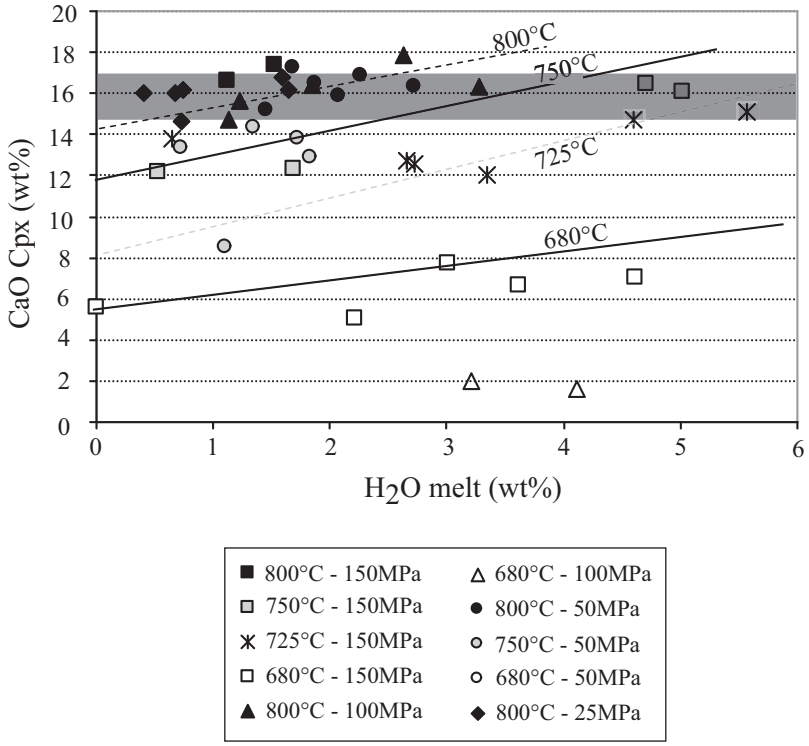

Fig. 8. Variation of the CaO content (wt %) of experimental clinopyroxenes with melt water content (H_2O_{melt}) at a range of temperatures and pressures. The grey band corresponds to the average CaO content of clinopyroxene phenocrysts in the starting rock.

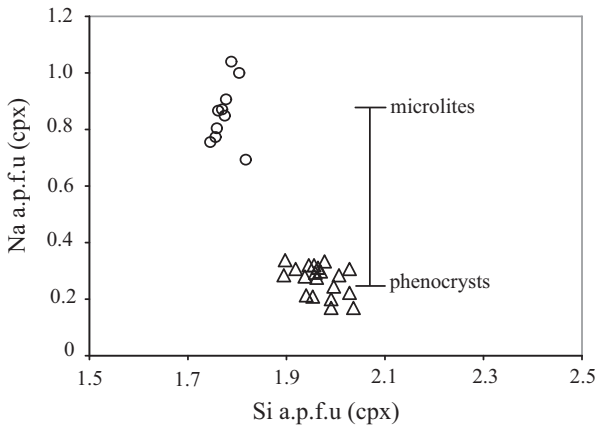

Fig. 9. Composition of experimental pyroxenes compared with that of pyroxene microlites and phenocrysts in the starting rock. Triangles, 800°C experiments; circles, 680°C experiments.

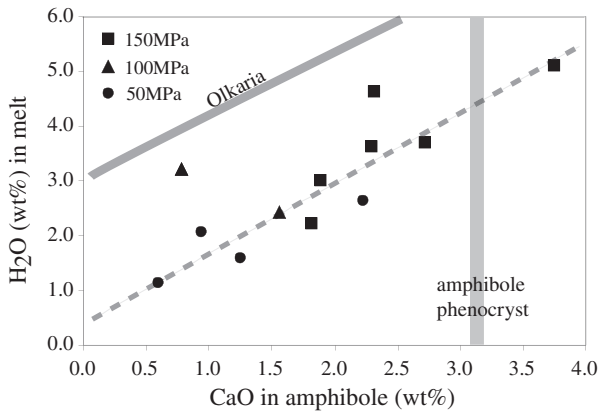

Fig. 10. Variation of the CaO wt % in the experimental amphiboles with melt water content (H_2O_{melt}). Also shown is the amphibole compositional trend obtained in the experimental study of Scaillet & Macdonald (2003) on the crystallization of Kenyan comendites (diagonal grey line labelled Olkaria). The vertical grey line corresponds to the average CaO content of amphibole phenocrysts in the Pantelleria starting rock. The dashed grey line is a visual fit of the Pantelleria data trend.

melt Al_2O_3 content increases and so its peralkalinity decreases (i.e. relative to that of the starting bulk-rock composition), clinopyroxene fractionation driving liquids progressively out from the pantellerite field toward the dividing line between comendite and pantellerite in the Macdonald (1974) projection (Fig. 11a). However, none of the experimental liquids produced either approach or even trend towards the comendite–trachyte field, suggesting that the such trachytic rocks are not directly parental to the dominant pantellerite variety.

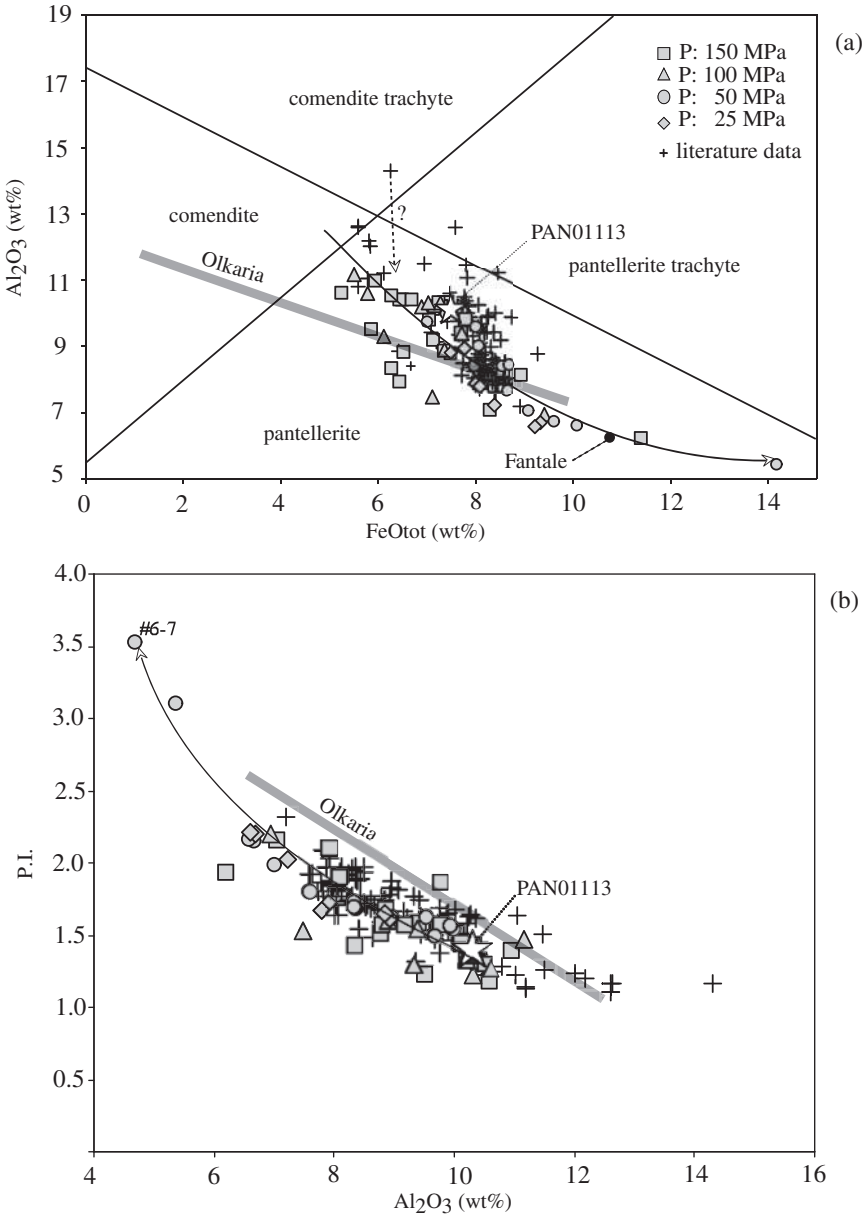

Fig. 11. Comparison between the experimental glasses and natural whole-rock compositions (a) Macdonald (1974) diagram [FeO_{tot} vs Al_2O_3 (wt %)] for peralkaline rocks. The vertical dashed line with a question mark indicates the hypothetical fractionation trend from a comendite trachytic parental magma towards the pantellerite field. (b) Al_2O_3 (wt %) vs peralkalinity index (P.I.). Crosses, literature whole-rock data; star, starting composition (PAN 01113); grey, experiments at different pressure (squares, 150 MPa; triangles, 100 MPa; circles, 50 MPa; diamonds, 25 MPa). Literature data were taken from Civetta *et al.* (1984, 1998), Esperança & Crisci (1995), Avanzinelli *et al.* (2004), Ferla & Meli (2006), Rotolo *et al.* (2007) and White *et al.* (2009). In both (a) and (b) the large white star shows the starting material, and the arrowed continuous line indicates the main evolutionary melt trend, as constrained by the experiments of this study. The thick grey lines labelled Olkaria correspond to the experimental trend obtained by Scaillet & Macdonald (2003) for the crystallization of Kenyan comendites. In (a), the black circle indicates the composition of Fantale obsidian.

DISCUSSION

Comparison with previous work and general implications

We start by comparing our phase equilibria with those established for other pantellerites and comendites under similar T, P, H_2O and fO_2 conditions. The most relevant points concern the crystallization sequence, as follows.

(1) For Eburru (Kenya) pantellerite (PI = 1·96) at 150 MPa, the crystallization sequence (from 830 to 650°C) is quartz, alkali feldspar, amphibole, Na-pyroxene (Scaillet & Macdonald, 2006).

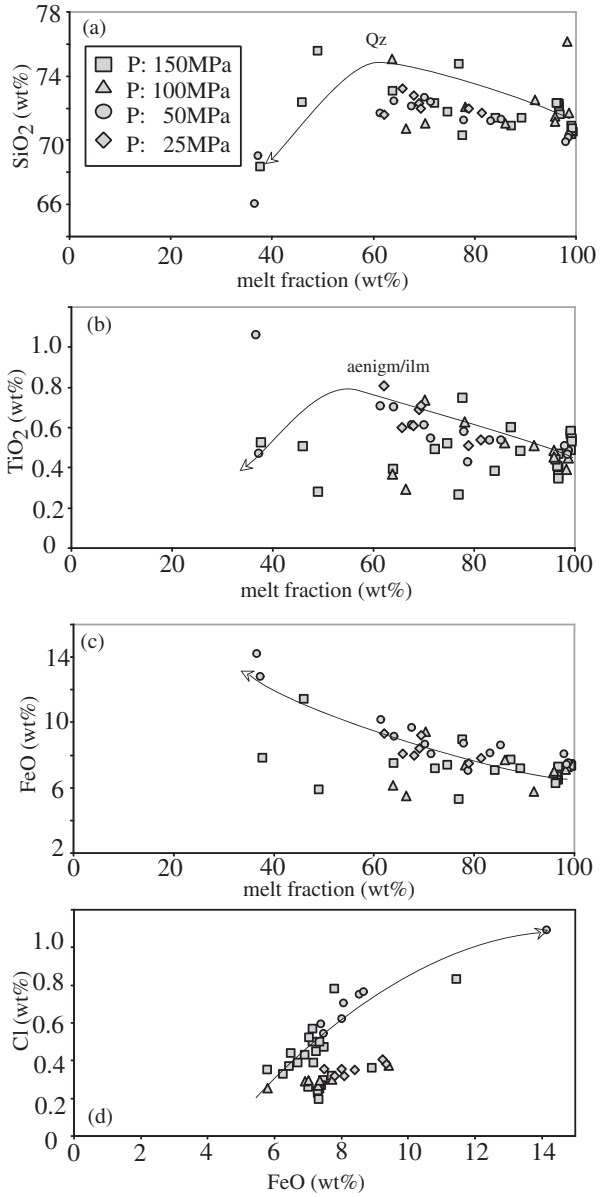

Fig. 12. Variation of selected oxides in the experimental glasses vs melt fraction (a–c) and of FeO vs Cl (d). The arrow indicates the trend of melt evolution. Symbols as in Fig. 11.

(2) For Olkaria (Kenya) comendite (PI = 1·36), at 150 MPa, the crystallization sequence (from 800 to 670°C) is Fe–Ti oxides, quartz + alkali feldspar, amphibole (sample BL 575, Scaillet & Macdonald, 2001, 2003).

(3) For Fastuca pantellerite (PI = 1·40), the crystallization sequence at 150 MPa (from 800 to 680°C) is clinopyroxene, alkali feldspar, aenigmatite, then amphibole and quartz, nearly simultaneously.

Both Eburru and Olkaria rhyolites are more silicic, with about 30% normative quartz compared with 24% for the Fastuca rock used in the present study, which accounts for the inversion between quartz and feldspar in the crystallization sequence. Similarly, the Fastuca pantellerite is slightly more CaO-rich compared with its Kenyan counterparts, which also explains the occurrence of calcic clinopyroxene in Pantelleria rhyolites and its absence in Kenyan strongly peralkaline felsic rocks with PI > 1·35 (clinopyroxene does occur in composition ND002 used by Scaillet & Macdonald (2001), which is at the boundary of the peralkaline field, PI = 1·02). With respect to amphibole, our results, along with those of Scaillet & Macdonald (2001, 2006), show that this mineral invariably occupies the low-temperature portion of the phase diagram, displaying a rather constant stability field in peralkaline rhyolites, from comendites (Scaillet & Macdonald, 2001) to pantellerites (Scaillet & Macdonald, 2006, present study). The occurrence of amphibole as phenocrysts in peralkaline silicic magmas thus indicates low-temperature conditions. A final point of interest is the aenigmatite stability field. Whereas crystallization of this mineral could not be achieved in experiments performed on Kenyan rhyolites (despite the fact that aenigmatite phenocrysts actually occur in the Kenyan rocks), our study had no particular problem in defining a stability field for this mineral. Our data show that near the liquidus aenigmatite requires melt peralkalinity higher than 1·2 and pressures ≥100 MPa. This latter point thus does not support the suggestion of Scaillet & Macdonald (2001) that aenigmatite crystallizes from peralkaline magmas only at $P < 100$ MPa. As noted above, the antipathetic occurrence of aenigmatite and Fe–Ti oxide suggests a reaction relationship between these phases (aenigmatite + O_2 = ilmenite + silica + Nds), as suggested by various researchers on the basis of their occurrence or textural evidence for reaction in natural pantellerite samples (e.g. Nicholls & Carmichael, 1969; White *et al.*, 2005; Rotolo *et al.*, 2007). Overall, this comparison shows clearly that, albeit small, the compositional differences existing between investigated felsic peralkaline rocks impart significant changes on phase topology. Thus, the use of the phase equilibrium data from this study to infer magmatic conditions for other peralkaline felsic systems should be done with caution.

As regards the composition of the melt phase, it should be noted that in experiments where pyroxene is the sole liquidus phase, the melt composition shows a clear decrease of its PI (to 1·20) with respect to the starting glass composition (the 'pyroxene effect', Scaillet & Macdonald, 2003). In other words, near-liquidus melts move towards less peralkaline comendite or trachyte compositions. On the contrary, in all those charges characterized by abundant alkali feldspar (as typical of natural pantellerites, R. Macdonald, personal communication) crystallization (i.e. lower temperature or lower H_2O_{melt}, except

charges 9-1 and 11-1), the melt PI increases steadily to values over two, owing to the less peralkaline character of the alkali feldspar relative to the coexisting melt (see also Scaillet & MacDonald, 2003). This trend of increasing peralkalinity may be halted only when a strongly sodic mineral, either amphibole or Na-rich clinopyroxene, enters the crystallization sequence.

Our work strengthens the observation that peralkaline rhyolites are characterized by low crystallization temperatures, in particular if they contain significant amounts of dissolved water, a point already made by Scaillet & Macdonald (2001, 2006). Metaluminous felsic magmas have their solidus temperature well approximated by that of the haplogranite system, for which the solidus at 150 MPa and H_2O saturation lies at around 680°C (Holtz *et al.*, 1992). The composition investigated here, along with those from Kenya, is still largely liquid at this temperature and H_2O-rich conditions, with the proportion of liquid over 90 wt %. For example, at H_2O saturation, run 4 (charge 4-1) at 725°C has 97 wt % liquid, whereas run 9 at 680°C (charge 9-1) has still 77 wt % residual liquid (Table 2). This peculiar behaviour implies that felsic peralkaline magma bodies emplaced in the cold upper crust will survive longer relative to their metaluminous equivalents, everything else being equal (i.e. host-rock temperature, volume of reservoir, thermal input by basaltic magma). From the chemical standpoint, the low solidus temperature of hydrous pantellerites illustrates that these felsic magmas have, upon cooling, a greater potential to produce extreme compositions relative to either metaluminous or peraluminous rhyolites, unless the latter have larger amounts of flushing elements such as fluorine or boron (e.g. Pichavant, 1987). As illustrated in Fig. 11, extreme fractionation of pantellerite yields liquids very rich in iron and alkalis.

There is little doubt that cooling peralkaline felsic magmas also produce such iron-rich liquids; however, these are not erupted or sampled by eruptive processes. The reason may lie in the molar volumes of oxide components that make up the bulk chemical variation of peralkaline felsic series. The molar volume of the Al_2O_3 oxide component is 37 cm^3 mol^{-1}, that of FeO 14 cm^3 mol^{-1} and that of SiO_2 27 cm^3 mol^{-1}, similar to that of Na_2O, 29 cm^3 mol^{-1} (Lange & Carmichael, 1990), at a reference temperature of 1400°C (changes in T will not affect the trend). During fractionation, owing to their similar molar volumes and molecular weights, density changes related to the increase in Na_2O and decrease in SiO_2 components broadly cancel out each other. In contrast, the strong decrease in the content of the light oxide Al_2O_3 renders the derivative liquids heavier, and this effect is exacerbated by the increase in the heavier FeO oxide that equally typifies peralkaline fractionation trends. Although such an increase in density may be partly offset by an increase in Fe_2O_3 (42 cm^3 mol^{-1}) and dissolved water, we tentatively suggest that the scarcity of perakaline rhyolites with iron contents significantly higher than 8–9 wt % is related to negative buoyancy effects arising from elevated dissolved iron in the melt.

Although our study is not directly aimed at constraining the origin of rhyolites at Pantelleria, the phase equilibria provided by our experiments do allow some insights into this aspect to be gained. White *et al.* (2009) have used MELTS and mass-balance arguments to constrain the various stages of magmatic differentiation which could have led to pantelleritic liquids (see also Civetta *et al.*, 1998; Avanzinelli *et al.*, 2004). As noted above, regardless of the dominant mechanism of differentiation being modelled, MELTS successfully reproduces the basalt to trachyte path, but fails to reproduce the most evolved, low-temperature, liquids, as documented here and by White *et al.* (2009). The mass-balance calculations provide, in contrast, useful indications: they show in particular that the 'last' magma differentiation stage (i.e. that from comendite–trachyte towards pantellerite) is characterized by a phase assemblage largely dominated by alkali feldspar and clinopyroxene, with olivine, ilmenite and apatite being present in minor proportions. Such a result is in good agreement with our phase equilibrium constraints, which show that both clinopyroxene and alkali feldspar are the dominant phases on the liquidus of peralkaline rhyolites at Pantelleria (Fig. 4). This topological arrangement is indeed compatible with the hypothesis that pantellerites are the liquid extract from a source saturated in clinopyroxene and alkali feldspar. The liquid compositional trend discussed above (Fig. 11) suggests, however, that the relationship between comendite trachyte and pantellerite is not direct, and requires one additional step, which is not constrained by the present experiments. A possibility is that comendite trachyte fractionates towards comendite (dashed arrow in Fig. 11a), which then produces pantellerite, but this must await future experimental investigations to be proved or disproved.

PRE-ERUPTIVE CONDITIONS OF THE 'FASTUCA' MAGMA

We now establish the pre-eruptive conditions of the Fastuca eruption by combining experimental and petrological data. The recent studies of White *et al.* (2005, 2009) showed that felsic magmas (i.e. with $SiO_2 > 67$ wt %) at Pantelleria record temperatures in the range 680–800°C, which match well with the crystallization interval established here for the Fastuca rhyolite (Fig. 4). It is worth stressing that several thermobarometers were applied by White *et al.* (2005), each based on different crystal–crystal (two oxides, clinopyroxene–olivine) or crystal–liquid (cpx–liquid, feldspar–liquid) equilibria. In the vast

majority of cases, temperature convergence was observed whenever these various techniques could be applied to a single sample, which supports the view that crystal–liquid equilibrium was closely approached in the corresponding magmas prior to eruption. Only a few exceptions to this behaviour were noted in some trachytic inclusions, which are not the focus of this study. Phase proportions obtained in our experiments agree closely with those observed in the natural rock, in particular with respect to the dominant phenocrysts, feldspar and clinopyroxene. Therefore, we conclude that our phase equilibrium data provide a good experimental framework for assessing the pre-eruptive conditions of recent felsic magmas at Pantelleria. Although in our work no effort was made to systematically vary the redox conditions, unlike a previous similar study (Scaillet & Macdonald, 2003), fO_2 changes arising from fH_2O variations are significant (Fig. 7). This provides constraints on the role of fO_2 on phase assemblages and compositions, and hence helps to assess pre-eruptive fO_2. In particular, the compositions of experimental ferro-magnesian minerals are all characterized by extremely iron-rich compositions, very close to those of the natural phenocrysts (Table 1). The immediate implication is that the fO_2 conditions applied to our experiments correctly mimic those of the magma reservoir, although, as discussed below, clinopyroxene might suggest slightly more reducing conditions. Altogether, this confirms the fO_2 estimates made by White *et al.* (2005, 2009) with respect to the reduced character of Pantelleria rhyolites (NNO − 1 to NNO − 2). In the discussion below we first consider constraints from melt inclusions combined with phase relationships to derive the most likely set of P–T–H_2O conditions that prevailed in the reservoir shortly before eruption, then use phase compositions to refine those estimates. We then evaluate whether the magma was fluid-saturated and discuss the composition of the fluid.

Phase equilibria and melt inclusion constraints

Several groups have analysed the volatile contents of melt inclusions (MI) trapped in pantellerite phenocrysts. Kovalenko *et al.* (1988) first analysed MI in anorthoclase and quartz by ion microprobe and found an H_2O_{melt} of about 4·3 ± 0·3 wt %. Lowenstern & Mahood (1991) performed systematic FTIR analyses of various quartz phenocrysts from the Green Tuff and found lower water contents, from 1·4 to 2·1 wt %; they contended that Kovalenko *et al.* (1988) overestimated H_2O_{melt} owing to analytical difficulties. Métrich *et al.* (2006) also analysed MI in quartz from 'the most recent Plinian eruption of Mt Grande' (we suppose that these workers referred to one of the Mida or Fastuca eruptions, which are not actually Plinian) and found an average H_2O_{melt} of 2·45 ± 0·25 wt %. In addition, Métrich *et al.* (2006) reported a homogenization temperature of about 740 ± 15°C, which they interpreted as the temperature of melt entrapment during quartz crystallization. Gioncada & Landi (2010) reported H_2O contents up to 4·4 wt % (mean values clustering at 2·5–4·3 wt %) in MI hosted in fayalite or feldspar from pantellerite tephra nearly contemporaneous with the Fastuca eruption. No CO_2 could be detected in any MI analysed by FTIR (Lowenstern & Mahood, 1991; Gioncada & Landi, 2010). Although these studies have analysed different eruptive units, which may explain part of the variability in H_2O_{melt}, their results suggest that the peralkaline rhyolites at Pantelleria achieve dissolved H_2O in the range 2–3 wt % by the time quartz crystallizes. The homogenization temperature reported by Métrich *et al.* (2006) broadly agrees with our phase relationships (Fig. 4), although our results suggest slightly lower temperatures (720°C at around 100 MPa) relative to that from the heating-stage measurement.

Geophysical studies suggest the existence of a magma reservoir at a depth of about 4 km, which corresponds to a lithostatic pressure slightly over 100 MPa for an average crustal density of 2·6 g cm^{-3} (Bonaccorso & Mattia, 2000; Mattia *et al.*, 2007). The main topological argument relevant to these pressure estimates comes from aenigmatite stability. Aenigmatite is not stable near the liquidus at pressures lower than 100 MPa, over the experimental temperature range investigated in this study. The ubiquitous occurrence of aenigmatite in the natural samples therefore sets a minimum pressure of 100 MPa for the magma reservoir feeding the recent felsic volcanism at Pantelleria. These findings corroborate the geophysical inferences and allow us to discuss the most probable T–H_2O pre-eruptive conditions on the basis of our phase equilibria determined at 100 and 150 MPa.

The phase relationships summarized in Fig. 13 are those of the 150 MPa section with superimposed curves of isocrystallinity of the experimental charges. Assuming a pre-eruptive melt H_2O content in the range 2–3 wt %, as suggested by the MI analyses, then the pre-eruptive temperature is essentially constrained by the stability field of quartz, from 720°C to 700°C. If amphibole is included, then slightly lower temperatures (~680°C) are needed. Carrying out the same exercise with the 100 MPa section yields essentially the same temperature range. At this pressure, however, melt water contents are constrained to be higher than 2·5 wt % for aenigmatite to crystallize. Conversely, amphibole is not stable at H_2O_{melt} over 4 wt % if stored at 100 MPa, which sets an upper bound in dissolved H_2O for pantellerites carrying this phenocryst. Overall, considering the full phenocryst assemblage, the topological arguments constrain the last equilibration temperatures of the magma to be in the range 680–720°C at rather H_2O-rich conditions, around 3–4 wt % H_2O_{melt}, outside the range given by MI in quartz, but within the high-H_2O range bracketed by the feldspar MI. The

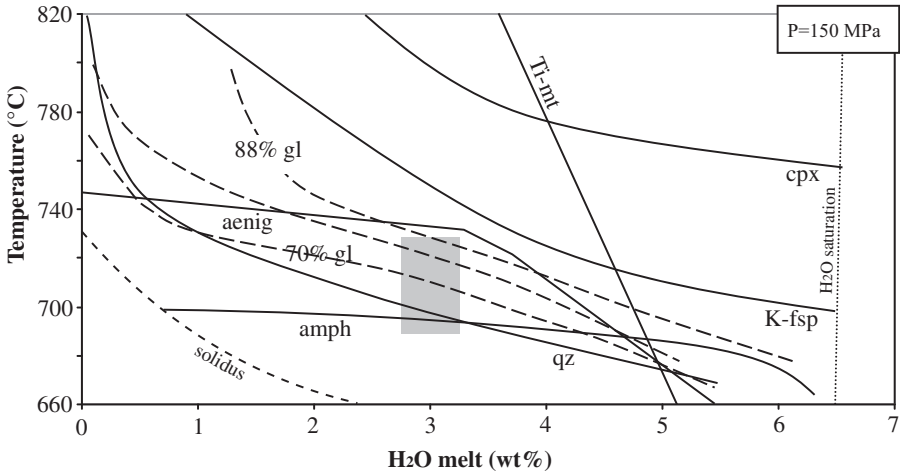

Fig. 13. Phase boundaries (continuous lines) at 150 MPa with superimposed isocrystallinity curves derived from the experiments (dashed lines). The range of water content of melt inclusions in alkali feldspar and aenigmatite (Gioncada & Landi, 2010) is indicated by the grey box at the inferred pre-eruptive temperature (see text).

generally low crystal content of the pantellerites argues for the pre-eruptive temperature being close to the upper end of that range. This is also borne out by the proportion of feldspar in the rock (13–14 wt %), which is also compatible with temperatures being around 720–750°C for this range of H_2O_{melt} (Fig. 2). We suggest that the (rare) occurrence of amphibole in the natural rocks, which is bracketed by our experiments in the low-*T* region, thus implying distinctly higher crystal contents than that of the natural sample, might be the result of crystal entrainment from cooler and more H_2O-rich portions of the tapped magma reservoir. We return to this point below.

Compositional constraints

Additional constraints on the pre-eruptive conditions come from the consideration of mineral compositions, in particular feldspar, clinopyroxene and amphibole, taking account of the effects of intensive variables on mineral chemistry as detailed above.

Feldspar phenocrysts and microlites have a rather homogeneous composition, at about Or_{36} (Table 1), which is compatible with a large range of H_2O_{melt} (Fig. 6), essentially from nearly dry to 4 wt % dissolved H_2O. Such a composition also indicates that the likely pre-eruptive temperature range is below 750°C. Temperatures significantly higher than 750°C are unable to produce the observed feldspar composition, regardless of H_2O_{melt}; under such conditions the crystallizing feldspar is always more sodic than Or_{35}. Alternatively, considering a temperature of magma storage at around 680°C would preclude H_2O_{melt} much higher than 2 wt %. However, such conditions (680°C and <2 wt % dissolved H_2O) would also imply a crystallinity much higher (i.e. >50 wt %; see Table 2) than observed (around 15–20 wt %). Therefore,

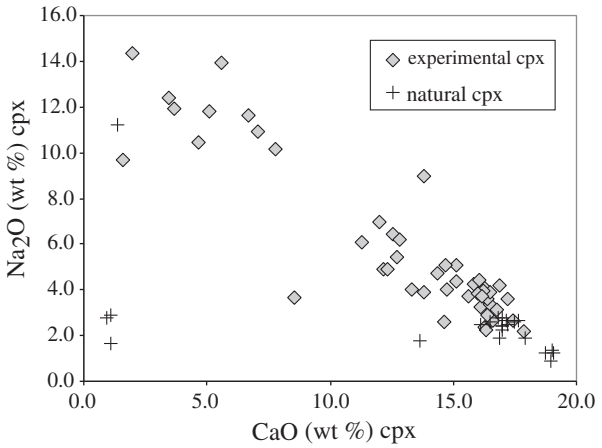

Fig. 14. Comparison between experimental (grey diamonds) and natural (crosses) clinopyroxenes in a Na_2O vs CaO (wt %) diagram.

when considered together with rock crystallinity, feldspar composition suggests that temperatures were closer to 720–750°C. Interestingly, it is in this temperature range that the feldspar composition varies little with H_2O_{melt}, which might explain the homogeneity already noted for this phase in Pantelleria rhyolites (e.g. White *et al.*, 2005; Ferla & Meli, 2006).

The experimental pyroxenes reproduce well those in the rock, bridging in particular the gap existing between calcium-poor and calcium-rich pyroxenes (Fig. 14). In detail, however, our experiments do not reproduce the Ca-rich end-member of the natural range (i.e. clinopyroxene with CaO higher than 18 wt %). These Ca-rich clinopyroxenes could reflect crystal inheritance from a parental mafic magma; however, their Fe/Mg is in equilibrium with groundmass ($Kd = 0{\cdot}17 \pm 0{\cdot}03$). In an XFe_{tot} vs

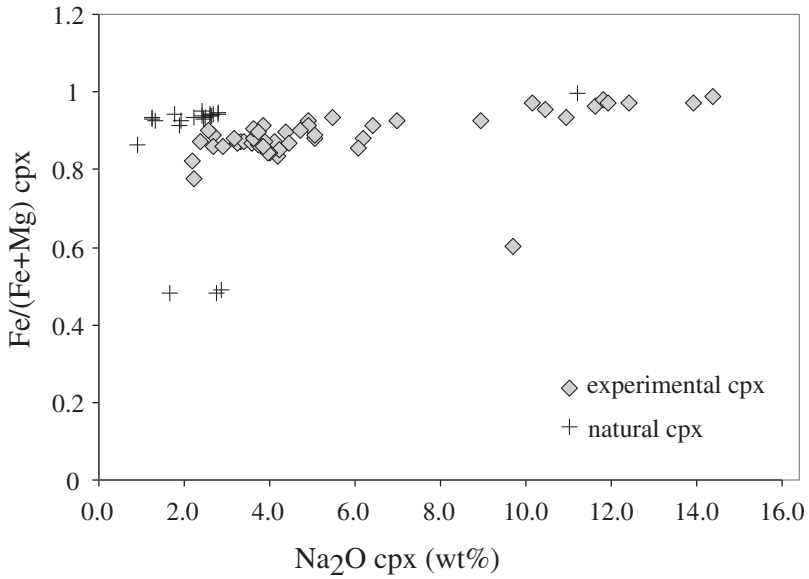

Fig. 15. Variation of Fe/(Fe + Mg) vs Na_2O (wt %) of natural and experimental clinopyroxenes. It should be noted that the former clinopyroxenes are slightly displaced toward higher *X*Fe values relative to the experimental clinopyroxenes with comparable Na contents.

Na_2O (wt %) plot, natural clinopyroxenes are displaced toward slightly higher XFe_{tot} values relative to the experimental pyroxenes with comparable Na contents (Fig. 15), which suggests that the natural redox conditions might have been slightly more reduced than in the experiments. Pre-eruptive temperatures may be obtained with our empirical calibration relating XFe_{tot} to temperature and fO_2. Use of such a correlation for the range of XFe_{tot} of the clinopyroxene phenocrysts (0·9–0·92) and assuming an fO_2 of NNO − 1·5 (White *et al.*, 2005, 2009) yields temperatures of 725–744°C, which overlap those indicated by feldspar (a change in 0·5 log unit in fO_2 affects these values by 12°C).

Constraints on H_2O_{melt} are provided by the CaO content of clinopyroxene. The common Ca-rich clinopyroxene in pantellerites has mostly around 15–17 wt % CaO (Fig. 14) (White *et al.*, 2005, 2009). According to the trends shown in Fig. 8, such a range in CaO requires an H_2O_{melt} of 3–5 wt % at 750°C, or 4–6 wt % at 725°C, considerably higher than the values determined from MI analyses hosted in quartz. In such a scheme, Ca-richer clinopyroxene (i.e. with > 18 wt % CaO) possibly records a high-temperature stage of magma crystallization, or inheritance from a more Ca-rich magma. In any case, the dominant calcic clinopyroxene composition points toward elevated H_2O content in the magma reservoir, in the range 3–6 wt %. The message delivered by feldspar led us to favour intermediate water contents, around 4 wt %. The very low content of MgO in the sodic variety of clinopyroxene (Table 1), which is minor in abundance compared with the Ca-rich variety, precludes an accurate estimate of its crystallization temperature. Our data can only be taken to indicate that such a sodic clinopyroxene grew at temperatures lower than 680°C. Only the experimental pyroxenes obtained at 680°C and 100 MPa approach the natural sodic clinopyroxene in terms of its CaO content (<2 wt %), confirming the low temperature estimates retrieved from their *X*Fe ratio. On this basis we suggest that sodic clinopyroxene records the last increment of magma crystallization, as inferred on textural grounds, possibly when cooling either during ascent in the conduit or after surface deposition of thick units.

All petrological studies carried out thus far on Pantelleria rhyolites have reported that the amphibole is a relatively rare mineral phase in erupted products (Civetta *et al.*, 1998; Avanzinelli *et al.*, 2004; White *et al.*, 2005; Ferla & Meli, 2006; Rotolo *et al.*, 2007); this indicates that, in most instances, the erupted magmas were only incipiently saturated in amphibole, if at all. In all of the above studies, the amphibole composition is characterized by CaO contents in the range 3·3–5·7 wt % (considering amphibole analyses from host-rocks having bulk CaO content similar to that of our starting material, Table 1). Our own amphibole has a CaO content of 3·3 wt % (Table 1), within the range of the other studies, implying a pre-eruptive dissolved H_2O content of around 4·5 wt %, according to the trend shown in Fig. 10. It is important to note that the more calcic amphiboles reported in other studies suggest even higher water contents, with H_2O_{melt} over 6 wt %; however, we recognize that such an estimate is beyond the calibrated range (0·41–5·68 wt % H_2O_{melt}). For example, the most calcic amphibole analysed by Avanzinelli *et al.*

(2004) in a pantellerite compositionally similar to that used in the present study (sample Pan 4), yields an H_2O_{melt} of *c.* 6·6 wt %. Conversely, there are no published amphibole analyses with less than 3 wt % CaO. Therefore, although amphibole is rare in the volcanic products at Pantelleria, its presence seems to trace back to more H_2O-rich conditions than the other phenocrysts, in particular quartz and alkali feldspar. Considering water solubility constraints (see Fig. 5), such water content estimates also require that the pressure of the magma storage zone extends up to at least 150 MPa.

Further constraints from amphibole and quartz

The above arguments show that the phase assemblage preserved by the rhyolite is broadly consistent with equilibrium crystallization at depth. Portions of the erupted magmas not saturated in amphibole, but carrying feldspar, clinopyroxene and aenigmatite, by far the dominant phenocryst mineralogy of rhyolites at Pantelleria (Rotolo *et al.*, 2007; White *et al.*, 2009), are consistent with conditions of last equilibration in the pressure range 100–150 MPa at around $730 \pm 10^{\circ}C$ and with about 4 wt % dissolved H_2O in the melt. The batches of amphibole-bearing magma require different conditions, however, as such amphibole is not stable under these T–H_2O_{melt} conditions. A puzzling aspect is the variability of retrieved pre-eruptive H_2O_{melt}, depending on which phase is being considered. In particular, quartz seems to record conditions no wetter than 3 wt % H_2O_{melt}, whereas amphibole consistently argues for H_2O_{melt} in the range 4–5 wt %. Such a difference is unexpected owing to the relatively late character of both phases in any isobaric crystallization sequence (Figs 4 and 5), at least under the explored conditions. A melt with 4·5 wt % dissolved H_2O requires a pressure of 100 MPa, but at this pressure amphibole is not stable at H_2O saturation (Fig. 4b); this therefore calls for higher pressures sufficient for amphibole to be stable under water-rich conditions (i.e. ~150 MPa). It should also be noted that, at a temperature lower than 700°C, the magma is almost always feldspar-saturated (Fig. 4), and the feldspar crystallizing from such H_2O-rich and cool melts can be much more potassic (up to Or_{50}, Fig. 6) than the preserved phenocrysts. Similarly, under these conditions clinopyroxene is much less calcic (<10 wt % CaO, Fig. 8) than in the natural rock. It is thus difficult to reproduce all the petrological characteristics within a single narrow P–T–H_2O_{melt} domain, when consideration is given to amphibole occurrence. We therefore tentatively suggest that amphibole represents crystals coming from a wetter and cooler, and possibly slightly deeper, region of the magma plumbing system, in which the phase relationships allowed amphibole crystallization without concomitant alkali feldspar and perhaps clinopyroxene precipitation [compare with the syneruptive mixing model invoked by Rotolo *et al.* (2007)]. The strong freezing point depression effect of water upon tectosilicate crystallization temperatures in silicate magmas makes such a scenario viable for feldspar. For clinopyroxene, the case is less clear. The continuous trend between sodic and calcic–sodic amphiboles shown in Fig. 10 and by Scaillet & Macdonald (2003) indicates that amphibole competes with clinopyroxene for Ca availability in the melt under water-rich conditions. If the trend shown here persists at higher pressure, we suggest that both phases may enter into a peritectic relationhip, to the point of only amphibole being stable near the liquidus, crystallizing before feldspar and replacing clinopyroxene. This could explain the occurrence of calcic amphibole and lack of potassic feldspar or intermediate sodic–calcic clinopyroxene. Such a hypothesis has still to be tested experimentally, however. It remains true that amphibole is a rare mineral in Pantelleria rocks, be it in lavas, pumices or in enclaves of inferred cumulative origin (never more than 3 vol. % in felsic enclaves hosted by pantellerites, Ferla & Meli, 2006). The last observation shows that conditions conducive to massive amphibole crystallization at depth, as attained in some of our charges (Table 2), are not widespread in the reservoir(s) feeding the silicic eruptions at Pantelleria. Another possibility to explain amphibole occurrence closer to the liquidus is that the magma is locally richer in fluorine, an element that is known to expand the thermal stability of amphibole and that occurs at the weight per cent level in some Pantelleria amphiboles (White *et al.*, 2005).

The information gained from MI in quartz also needs further discussion. As noted above, melt inclusion studies at Pantelleria have concentrated on quartz, although this phase does not always occur in the common phenocryst assemblage of pantellerites, and when present is sometimes described as having embayed shapes (e.g. Avanzinelli *et al.*, 2004). The water contents in quartz-hosted melt inclusions are never higher than 2·5 wt %. Assuming as a starting point the pre-eruptive conditions derived above for the feldspar–clinopyroxene–aenigmatite assemblage (150 MPa, $730 \pm 10^{\circ}C$ and *c.* 4 wt % H_2O_{melt}) and considering the case of closed-system crystallization, it is difficult to attain isobaric conditions under which quartz would grow from a melt with 2·5 wt % dissolved H_2O, unless the system lost water upon cooling. Even if this were the case, the end result would be a magma having a much higher crystal load than observed and with amphibole having significantly less CaO than the actual phenocrysts. The simplest alternative is to assume polybaric, instead of isobaric, crystallization, such that a magma at 720–730°C grows quartz on its ascent towards the surface when intercepting the quartz-in temperature (Fig. 5). The pressure at which quartz starts growing will depend on the amount of dissolved water remaining in the liquid, which will be in turn be controlled by the composition and abundance of

any coexisting fluid phase in the reservoir (see below). Such a scenario could explain the range of H_2O_{melt} reported by previous workers, and the fact that quartz records relatively less hydrous conditions compared with the other phenocrysts. Alternatively, a slight increase in the magma silica content, relative to that of our starting material, may raise the quartz in-curve to higher temperatures, as evidenced by the comparison between Kenyan and Pantelleria rhyolites mentioned above. This could explain the greater abundance of quartz in other Pantelleria rhyolites.

The emerging picture is thus one in which the bulk of the crystallization occurs isobarically in a shallow magma reservoir in the pressure range 100–150 MPa, at a pre-eruptive temperature of around 730 ± 10°C, with a melt water content of about 4 wt %. These conditions fulfil all the petrological constraints brought about by the coexistence, relative proportions, and compositions of the predominant phase assemblage in the Pantelleria rhyolites (feldspar, clinopyroxene ± aenigmatite). In addition to the compositional effects, the occurrence of other, minor, phases requires either higher (amphibole) or lower (quartz, aegirine microlites) saturation pressures, which are possibly related to the dynamics of the plumbing system during, or prior to, eruptive events.

Fluid phase: inferences on its presence and composition

Experimental H_2O solubility experiments carried out on the same starting composition as in this study (Di Carlo *et al.*, in preparation) indicate that for an H_2O_{melt} close to 4 wt %, exsolution is expected at a pressure of 80 MPa. This is based upon the premise that the sole volatile present is water. However, the fact that FTIR analyses could not detect any dissolved CO_2 in MI cannot be taken as an evidence for the lack of this species in the system, but only to indicate that if present, the amount of CO_2 dissolved is below the FTIR detection level (<50 ppm). Our own analyses of some near-liquidus CO_2-bearing charges revealed the lack of detectable dissolved CO_2 in the melt (charges 5-2, 8-2, 8-3 and 8-4). Another volatile species present in appreciable concentrations is chlorine (Lowenstern, 1994), with up to 1 wt % dissolved Cl. Although it is well established that the propensity for Cl degassing is much lower in peralkaline than in metaluminous magmas (e.g. Métrich & Rutherford, 1992), Cl analyses of MI in Pantelleria phenocrysts led Lowenstern (1994) to conclude that pantellerite silicic magmas were saturated in brine at their level of storage, and that an H_2O-rich and Cl-poor fluid was also present in the reservoir. That the Pantellera rhyolites were vapour-saturated at depth is also indicated by the behaviour of Cu, which has been interpreted as reflecting strong Cu partitioning into a fluid phase prior to eruption (Lowenstern *et al.*, 1991). These lines of evidence suggest that the magmas were fluid-saturated prior to eruption and that our pre-eruptive H_2O_{melt} thus represents only a minimum estimate of the total amount of water present in the magma. The amount of exsolved water is unknown but we may rely on evidence gathered from other locations (Scaillet *et al.*, 2003; Scaillet & Pichavant, 2005). The restoration of the amount of exsolved fluid in magma chambers in a variety of tectonic settings shows that most upper crustal magma reservoirs contain up to 5 wt % exsolved fluid (Scaillet *et al.*, 2003). Under these conditions, if this exsolved fluid was dominated by water (i.e. with an $XH_2O_{fluid} > 0{\cdot}8$), as implied by our phase equilibrium constraints and suggested by the lack of dissolved CO_2 in the melt inclusions, then it appears that the bulk amount of water present in the pantellerite magmas could be as much as twice that dissolved in the silicate melt.

In view of the possibility of having fluid-saturated conditions in the silicic reservoir, the next important point to be addressed is the composition of such deep fluids. The constraints on pre-eruptive P–T–H_2O_{melt}–fO_2 (this study; White *et al.*, 2005, 2009) allow us to infer the gross chemical characteristics of the fluid likely to escape the reservoir as a precursor to magma ascent. Perhaps the most salient point is the fact that the pre-eruptive melt is both reduced and water-rich, which in turn implies that any coexisting fluid phase will be also H_2O- and H_2-rich. The amounts of H_2O and H_2 in the fluid can be estimated using the following standard thermodynamic relationship, which relates species fugacity f_i to its mole fraction, X_i:

$$f_i = X_i \gamma_i P_{tot}$$

γ_i being the fugacity coefficient of the relevant species and P_{tot} the total pressure. We use this empirical activity–composition relationship for water in pantellerite to derive fH_2O. Then, based on the fO_2 determined from the phenocryst assemblage (*c.* NNO − 1·5, White *et al.*, 2009), we calculate the corresponding fH_2, using the water dissociation equilibrium as explained above. The fugacity coefficients of H_2O and H_2 at P and T are from Burnham *et al.* (1969) and Shaw & Wones (1964), respectively. A magma with 4 wt % dissolved H_2O at 730°C and 150 MPa and NNO − 1·5 would coexist with a fluid phase with $XH_2O = 0{\cdot}78$ and $XH_2 = 0{\cdot}012$, the rest being made of carbon- and sulphur-bearing species and/or halogens. Decreasing fO_2 to NNO − 2 would only marginally increase XH_2 ($=0{\cdot}021$), whereas increasing fO_2 to NNO, an fO_2 typical of arc environments, would led to a dramatic decrease in XH_2, by an order of magnitude ($=0{\cdot}002$). Decreasing pressure to 120 MPa merely increases XH_2O ($=0{\cdot}97$), XH_2 remaining at the same level ($=0{\cdot}015$). These calculations show, therefore, that any currently existing peralkaline felsic reservoir beneath Pantelleria will probably release fluids whose key chemical characteristics will be their abundance in hydrogen-bearing species, including significant levels of H_2, and also their CO_2-poor character.

The fluid will also contain a certain amount of halogens, in particular F and Cl; however, these two elements strongly favour the melt over the gas phase in peralkaline systems (Carroll & Webster, 1994), hence we anticipate that their contribution to the gas phase leaving the reservoir is minimal.

These H_2-rich conditions, if typical of peralkaline reservoirs elsewhere, may explain one often noted peculiarity of plutonic alkali-rich felsic bodies. Detailed petrological studies have indeed reported an increase in fO_2 during cooling in several syenite–alkaline granite complexes (see Marks *et al.*, 2003), one of the most diagnostic mineralogical associations being the replacement of arfvedsonite by aegirine, which can be related to a redox reaction. The richness in H_2 of magmatic fluids documented here offers one possible explanation for such an evolution, namely oxidation via preferential loss of H_2 relative to other volatile species. It has been long proposed (Sato, 1978) that H_2 might diffuse out magma bodies at a rates comparable with that of heat loss owing to its elevated mobility (Gaillard *et al.*, 2003), thereby oxidizing the melt or its crystallization products during cooling. We suggest that such a process is very efficient in peralkaline magmas, at least those that are water-rich and reduced, which imposes elevated H_2 contents in the coexisting fluid phase.

CONCLUSIONS

This study was aimed at exploring the phase relations and compositions of a hydrous pantellerite system to constrain the pre-eruptive conditions (T, P and H_2O_{melt}) of pantelleritic magma erupted during the most powerful eruption of the last 45 kyr at Pantelleria island. The P–T–H_2O grid derived from this study is composition-specific (i.e. can be applied only to similar mildly evolved pantelleritic systems), but has allowed us to assess the pre-eruptive conditions of this particular pantelleritic eruption, given that mineral phase assemblage and phase composition, melt included, are well characterized. Our results suggest that the depth of magma storage prior to the eruption of the Fastuca magma can be set at around 4 km (i.e. at a pressure around 120 MPa), in good agreement with geodetic constraints (Mattia *et al.*, 2007). Magma temperatures can be constrained to between 680 and 720°C, with an H_2O content in the melt of around 4 wt %. These rather H_2O-rich conditions for the Fastuca magma seem to be common to coeval, but lower energy strombolian pantelleritic pumice eruptions (on the basis of continuing melt inclusion studies, P. Landi, personal communication). However, future work will have to demonstrate whether the H_2O-rich character as determined here is representative of all of the recent silicic magmatism at Pantelleria. Our work also shows that inference of pre-eruptive volatile contents obtained only from melt inclusion analyses may lead to significant errors, if not interpreted in the context of crystal–liquid equilibrium.

ACKNOWLEDGEMENTS

We are grateful to Patrizia Landi, Ray Macdonald and John White for their thorough and extremely constructive reviews, which much improved the original manuscript, and to Marjorie Wilson for the careful editorial handling.

FUNDING

This study was partly funded by a project of the Italian Istituto Nazionale di Geofisica e Vulcanologia and Dipartimento Protezione Civile (INGV-DPC project, 2004–2006, V3-07, Pantelleria).

REFERENCES

Albarède, F. (1995). *Introduction to Geochemical Modeling*. Cambridge: Cambridge University Press, 543 p.

Avanzinelli, R., Bindi, L., Menchetti, S. & Conticelli, S. (2004). Crystallization and genesis of peralkaline magmas from Pantelleria volcano: an integrated petrological and crystal-chemical study. *Lithos* **73**, 41–69.

Bailey, D. K. & Macdonald, R. (1987). Dry peralkaline felsic liquids and carbon dioxide flux through the Kenya rift zone. In: Mysen, B. (ed.) *Magmatic Processes: Physicochemical Principles. Geochemical Society, Special Publication* **1**, 91–105.

Barclay, J., Carroll, M. R., Houghton, B. F. & Wilson, C. J. N. (1996). Preeruptive volatile content and degassing history of an evolving peralkaline volcano. *Journal of Volcanology and Geothermal Research* **74**, 75–87.

Bohrson, W. A. & Reid, M. R. (1997). Genesis of silicic peralkaline volcanic rocks in an ocean island setting by crustal melting and open-system processes: Socorro Island, Mexico. *Journal of Petrology* **38**, 1137–1166.

Bogaerts, M., Scaillet, B. & Vander Auwera, J. (2006). Phase equilibria of the Lyngdal granodiorite (Norway): implications for the origin of metaluminous ferroan granitoids. *Journal of Petrology* **12**, 2405–2431.

Bonaccorso, A. & Mattia, M. (2000). Deflation acting on island of Pantelleria inferred through geodetic data. *Earth and Planetary Letters* **180**, 91–101.

Burnham, C. W., Holloway, J. R. & Davis, N. F. (1969). Thermodynamic properties of water to 1000°C and 10000 bars. *Geological Society of America, Special Papers* **132**, 1–96.

Carroll, M. J. & Webster, J. (1994). Solubilities of sulfur, noble gases, nitrogen, chlorine, and fluorine in magmas. In: Carroll, M. R. & Holloway, J. R. (eds) *Volatiles in Magmas. Mineralogical Society of America, Reviews in Mineralogy* **30**, 231–271.

Caricchi, L., Ulmer, P. & Peccerillo, A. (2006). A high-pressure experimental study on the evolution of the silicic magmatism of the main Ethiopian Rift. *Lithos* **91**, 46–58.

Civetta, L., Cornette, Y., Crisci, G., Gillot, P. Y., Orsi, G. & Requejo, C. S. (1984). Geology, geochronology and chemical evolution of the island of Pantelleria. *Geological Magazine* **121**, 541–562.

Civetta, L., D'antonio, M., Orsi, G. & Tilton, G. R. (1998). The geochemistry of volcanic rocks from Pantelleria Island, Sicily Channel: petrogenesis and characteristics of the mantle source region. *Journal of Petrology* **39**, 1453–1491.

Costa, F., Scaillet, B. & Pichavant, M. (2004). Petrological and experimental constraints on the pre-eruption conditions of Holocene dacite from Volcán San Pedro (36°S, Chilean Andes) and the importance of sulphur in silicic subduction-related magmas. *Journal of Petrology* **45**, 855–881.

Dall'Agnol, R., Scaillet, B. & Pichavant, M. (1999). An experimental study of a lower Proterozoic A-type granite from the eastern Amazonian craton, Brazil. *Journal of Petrology* **40**, 1673–1698.

Devine, J. D., Gardner, J. E., Brack, H. P., Layne, G. D. & Rutherford, M. J. (1995). Comparison of microanalytical methods for estimating H_2O contents of silicic volcanic glasses. *American Mineralogist* **80**, 319–328.

Esperança, S. & Crisci, G. M. (1995). The island of Pantelleria: a case of DMM–HIMU isotopic compositions in a long-lived extensional setting. *Earth and Planetary Science Letters* **136**, 167–182.

Ferla, P. & Meli, C. (2006). Evidence of magma mixing in the 'Daly gap' of alkaline suites: a case study from the enclaves of Pantelleria (Italy). *Journal of Petrology* **147**, 1467–1507.

Gaillard, F., Burkhard, S., Mackwell, S. & McCammon, C. (2003). Rate of hydrogen–iron exchange in silicate melts and glasses. *Geochimica et Cosmochimica Acta* **67**, 2427–2441.

Gioncada, A. & Landi, P. (2010). The pre-eruptive volatile contents of recent basaltic and pantelleritic magmas at Pantelleria (Italy). *Journal of Volcanology and Geothermal Research* **189**, 191–201.

Holtz, F., Pichavant, M., Barbey, P. & Johannes, W. (1992). Effects of H_2O on liquidus phase relations in the haplogranite system at 2 and 5 kbar. *American Mineralogist* **77**, 1223–1241.

Klimm, K., Holtz, F., Johannes, W. & King, P. L. (2003). Fractionation of metaluminous A-type granites: an experimental study of the Wangrah Suite, Lachlan Fold Belt, Australia. *Precambrian Research* **124**, 327–341.

Kovalenko, V. I., Hervig, R. L. & Sheridan, M. F. (1988). Ion-microprobe analyses of trace elements in anorthoclase, hedenbergite, aenigmatite, quartz, apatite and glass in pantellerite: evidence for high water contents in pantellerite melts. *American Mineralogist* **73**, 1038–1045.

Lange, R. & Carmichael, I. S. E. (1990). Thermodynamics properties of silicate liquids with emphasis on density, thermal expansion and compressibility. In: Nicholls, J. & Russel, J. K. (eds) *Understanding Magmatic Processes. Modern Methods in Igneous Petrology. Mineralogical Society of America, Reviews in Mineralogy* **24**, 25–64.

Leake, B. E. (1997). Nomenclature of amphiboles. Report of the subcommittee on amphiboles of the International Commission on new minerals and mineral names. *European Journal of Mineralogy* **9**, 623–651.

Lindsley, D. H. (1983). Pyroxene thermometry. *American Mineralogist* **68**, 477–493.

Lowenstern, J. B. (1994). Chlorine, fluid immiscibility, and degassing in peralkaline magmas from Pantelleria, Italy. *American Mineralogist* **79**, 353–369.

Lowenstern, J. B. & Mahood, G. A. (1991). New data on magmatic H_2O contents of pantellerites, with implications for petrogenesis and eruptive dynamics at Pantelleria. *Bulletin of Volcanology* **54**, 78–83.

Lowenstern, J. B., Mahood, G. A., Rivers, M. L. & Sutton, S. R. (1991). Evidence for extreme partitioning of copper into a magmatic vapor phase. *Science* **252**, 1405–1409.

Macdonald, R. (1974). Nomenclature and petrochemistry of the peralkaline oversaturated extrusive rocks. *Bulletin of Volcanology* **38**, 498–505.

Macdonald, R., Belkin, H. E., Fitton, J. G., Rogers, N. W., Nejbert, K., Tindle, A. G. & Marshall, A. S. (2008). The roles of fractional crystallization, magma mixing, crystal mush remobilization and volatile melt interactions in the genesis of a young basalt peralkaline rhyolite suite, the Greater Olkaria Volcanic Complex, Kenya Rift Valley. *Journal of Petrology* **49**, 1515–1547.

Mahood, G. A. (1984). Pyroclastic rocks and calderas associated with strongly peralkaline magmatism. *Journal of Geophysical Research* **89**, 8540–8552.

Mahood, G. A. & Hildreth, W. (1986). Geology of the peralkaline volcano at Pantelleria, Strait of Sicily. *Bulletin of Volcanology* **48**, 143–172.

Marks, M., Vennemann, T. W., Siebel, W. & Markl, G. (2003). Quantification of magmatic and hydrothermal processes in a peralkaline syenite–alkali granite complex based on textures, phase equilibria, and stable and radiogenic isotopes. *Journal of Petrology* **44**, 1247–1280.

Marshall, A. S., Hinton, R. W. & Macdonald, R. (1998). Phenocrystic fluorite in peralkaline rhyolites, Olkaria, Kenya rift valley. *Mineralogical Magazine* **62**, 477–486.

Marshall, A. S., MacDonald, R., Rogers, N. W., Fitton, J. G., Tindle, A. G., Nejbert, K. & Hinton, R. W. (2009). Fractionation of peralkaline silicic magmas: the Greater Olkaria Volcanic complex, Kenya Rift Valley. *Journal of Petrology* **50**, 323–359.

Martel, C., Pichavant, M., Holtz, F., Scaillet, B., Bourdier, J.-L. & Traineau, H. (1999). Effects of fO_2 and H_2O on andesite phase relations between 2 and 4 kbar. *Journal of Geophysical Research* **104**, 29453–29470.

Mattia, M., Bonnacorso, A. & Guglielmino, F. (2007). Ground deformations in the island of Pantelleria (Italy): insights into the dynamic of the current intereruptive period. *Journal of Geophysical Research* **112**, doi:10.1029/2006JB004781.

Metrich, N. & Rutherford, M. (1992). Experimental study of chlorine behavior in hydrous silicic melts. *Geochimica et Cosmochimica Acta* **56**, 607–616.

Métrich, N., Susini, J., Foy, E., Farges, F., Massare, D., Sylla, L., Lequien, S. & Bonin-Mossba, M. (2006). Redox state of iron in peralkaline rhyolitic glass/melt X-ray absorption micro-spectroscopy experiments at high temperature. *Chemical Geology* **231**, 350–363.

Nekvasil, H., Dondolini, A., Horn, J., Filiberto, J., Long, H. & Lindsley, D. H. (2004). The origin and evolution of silica-saturated alkalic suites: an experimental study. *Journal of Petrology* **45**, 693–721.

Nicholls, J. & Carmichael, I. S. E. (1969). Peralkaline acid liquids: a petrological study. *Contributions to Mineralogy and Petrology* **20**, 268–294.

O'Neill, H. St. C. & Pownceby, M. I. (1993). Thermodynamic data from redox reactions at high temperature: I. An experimental and theoretical assessment of the electrochemical method using stabilized zirconia electrolytes, with revised values for Fe-"FeO"-, Co-CoO, Ni-NiO, an Cu-CuO2 oxygen buffers and new data for the W-WO2 buffer. *Contributions to Mineralogy and Petrology* **114**, 296–314.

Orsi, G., Ruvo, L. & Scarpati, C. (1989). The Serra della Fastuca Tephra at Pantelleria: physical parameters for an explosive eruption of peralkaline magma. *Journal of Volcanology and Geothermal Research* **39**, 55–60.

Papale, P., Neri, A. & Macedonio, G. (1998). The role of magma composition and water content in explosive eruptions: 1. Conduit ascent dynamics. *Journal of Volcanology and Geothermal Research* **87**, 75–93.

Pichavant, M. (1987). Effects of B and H_2O on liquidus phase relations in the haplogranite system at 1 kbar. *American Mineralogist* **72**, 1056–1070.

Pichavant, M., Costa, F., Burgisser, A., Scaillet, B., Martel, C. & Poussineau, S. (2007). Equilibration scales in silicic to intermediate

magmas—implications for experimental studies. *Journal of Petrology* **48**, 1955–1972.

Pownceby, M. I. & O'Neill, H. St. C. (1994). Thermodynamic data from redox reactions at high temperatures. III. Activity–composition relations in Ni–Pd alloys from EMF measurements at 850–1250 K and calibration of the NiO + Ni–Pd assemblage as a redox sensor. *Contributions to Mineralogy and Petrology* **116**, 327–339.

Robie, R. A., Hemingway, B. S. & Fisher, J. R. (1979). *Thermodynamic properties of minerals a,d related substances at 298·15 K and 1 bar (105 Pascals) pressure and at higher temperature. US Geological Survey Bulletin* **1452**.

Rotolo, S. G., Castorina, F., Cellura, D. & Pompilio, M. (2006). Petrology and geochemistry of submarine volcanism in the Sicily Channel Rift. *Journal of Geoogy* **114**, 355–365.

Rotolo, S. G., La Felice, S., Mangalaviti, A. & Landi, P. (2007). Geology and petrochemistry of recent (<25 ka) silicic volcanism at Pantelleria Island. *Bollettino della Società Geologica Italiana* **126**, 191–208.

Sato, M. (1978). Oxygen fugacity of basaltic magmas and the role of gas-forming elements. *Geophysical Research Letters* **5**, 447–449.

Scaillet, B., Pichavant, M. & Roux, J. (1995). Experimental crystallization of leucogranite magmas. *Journal of Petrology* **36**, 663–705.

Scaillet, B. & Evans, B. W. (1999). The 15 June 1991 eruption of Mount Pinatubo. I. Phase equilibria and pre-eruption P–T–fO_2–fH_2O conditions of the dacite magma. *Journal of Petrology* **40**, 381–411.

Scaillet, B., Luhr, J. F. & Carroll, M. (2003). Petrological and volcanological constraints on volcanic sulfur emissions to the atmosphere. In: Robock, A. & Oppenheimer, C. (eds) *Volcanism and the Earth's Atmosphere. Geophysical Monograph, American Geophysical Union* **139**, 11–40.

Scaillet, B. & Macdonald, R. (2001). Phase relations of peralkaline silicic magmas and petrogenetic implications. *Journal of Petrology* **42**, 825–845.

Scaillet, B. & Macdonald, R. (2003). Experimental constraints on the relationships between peralkaline rhyolites of the Kenya Rift Valley. *Journal of Petrology* **94**, 1867–1894.

Scaillet, B. & Macdonald, R. (2006). Experimental and thermodynamic constraints on the sulphur yield of peralkaline and metaluminous silicic flood eruptions. *Journal of Petrology* **47**, 1413–1437.

Scaillet, B., Pichavant, M., Roux, J., Humbert, G. & Lefèvre, A. (1992). Improvements of the Shaw membrane technique for measurement and control of fH_2 at high temperatures and pressures. *American Mineralogist* **77**, 647–655.

Scaillet, B. & Pichavant, M. (2005). A model of sulphur solubility for hydrous mafic melts: application to the determination of magmatic fluid compositions of Italian volcanoes. *Annals of Geophysics* **48**, 671–698.

Schmidt, B. C., Scaillet, B. & Holtz, F. (1995). Accurate control of fH_2 in cold seal pressure vessels with the Shaw membrane technique. *European Journal of Mineralogy* **7**, 893–903.

Shaw, H. R. & Wones, D. R. (1964). Fugacity coefficients for hydrogen gas between 0 and 1000°C, for pressures to 3000 atm. *American Journal of Science* **262**, 918–929.

Villari, L. (1974). The island of Pantelleria. *Bulletin of Volcanology* **38**, 680–724.

Webster, J. D., Holloway, J. R. & Hervig, R. L. (1987). Phase equilibria of a Be, U and F-enriched vitrophyre from Spor Mountain, Utah. *Geochimica et Cosmochimica Acta* **51**, 389–402.

Webster, J. D., Taylor, R. P. & Bean, C. (1993). Pre-eruptive melt composition and constraints on degassing of a water-rich pantellerite magma, Fantale volcano, Ethiopia. *Contributions to Mineralogy and Petrolog* **114**, 53–62.

White, J. C., Ren, M. & Parker, D. F. (2005). Variation in mineralogy, temperature, and oxygen fugacity in a suite of strongly peralkaline lavas and tuffs, Pantelleria, Italy. *Canadian Mineralogist* **43**, 1331–1347.

White, J. C., Parker, D. F. & Ren, M. (2009). The origin of trachyte and pantellerite from Pantelleria, Italy: insights from major element, trace element, and thermodynamic modelling. *Journal of Volcanology and Geothermal Research* **179**, 33–55.

Wilding, M. C., MacDonald, R., Davies, R. & Fallick, A. E. (1993). Volatile characteristics of peralkaline rhyolites from Kenya: an ion microprobe, infrared sspectroscopy and hydrogen isotope study. *Contributions to Mineralogy and Petrology* **114**, 264–275.